1 **Physical Drivers and Parameter Sensitivities of Pearl**

2 **River-derived Sediment Dispersal on the Northern South China**

3 **Sea Shelf: A modeling study**

4 ~~Modeling dispersal of the Pearl River-derived sediment over the~~

5 ~~Shelf~~

6 Guang Zhang[1,2,3], Suan Hu[1,2,3], Xiaolong Yu[1,2,3], Heng Zhang[1,2,3], Wenping Gong[1,2,3]*

7 [1] School of Marine Sciences, Sun Yat-sen University, Zhuhai, 519082, China

8 [2] Guangdong Provincial Key Laboratory of Marine Resources and Coastal Engineering, Zhuhai, 519082, China

9 [3] Pearl River Estuary Marine Ecosystem Research Station, Ministry of Education, Zhuhai 519082, China

10 Corresponding author: Wenping Gong (gongwp@mail.sysu.edu.cn)

Abstract

This study employs the Coupled-Ocean-Atmosphere-Wave-Sediment-Transport (COAWST) modeling system to quantitatively assess the seasonal suspension, transport, and annual fate of Pearl River-derived sediment (riverine slow-settling single fine grains and high-settling flocs) on the northern continental shelf of the South China Sea (SCS). Following careful model validation, a series of sensitivity experiments were conducted to investigate the effects of tides, waves, background circulation, sediment settling velocity, critical shear stress, and sediment spin-up durations. The results reveal strong seasonal variations in sediment dynamics driven by the East Asian monsoon. During the wet summer, weaker hydrodynamic conditions promote the initial deposition of riverine sediment via the surface buoyant plume. In contrast, stronger winds and waves during winter enhance sediment resuspension and southwestward transport, particularly toward the Beibu Gulf. Spatially, approximately two-thirds of the annual Pearl River-derived sediment load is retained near the estuary. About 9% reaches the continental shelf east of the PRE, while similar proportions accumulate in the Beibu Gulf and south of Hainan Island. Sensitivity experiments highlight the distinct and significant roles of different physical forcings in sediment dispersal. Tidal dynamics strongly enhance sediment mobilization and transport within the estuary by increasing bottom shear stress, which promotes offshore sediment export and limits local deposition. Wave forcing plays a dominant role in sediment

resuspension near the river mouth and along the coast, especially during winter, facilitating sediment redistribution across the shelf. ~~Excluding waves leads to greater sediment retention near the estuary and diminished transport toward distant regions.~~ The remotely forced (large-scale, non-local forcing) ambient shelf ~~Ambient~~ circulation~~, particularly~~ in summer~~,~~ drives ~~is essential for~~ eastward sediment transport, enabling sediment to spread widely across the shelf~~; when it is omitted, northeastward dispersal is greatly diminished~~. Model outcomes are also sensitive to sediment parameterization. The natural seasonal increase in critical shear stress for erosion during winter counteracts part of the wave-enhanced resuspension capacity, thereby reducing resuspension and erosion on the continental shelf east of ~~Using non-seasonal critical shear stress for erosion increases wintertime sediment mobility east of~~ the Leizhou Peninsula. Higher settling velocities decrease suspended sediment concentrations and promote near-source retention, limiting long-distance transport. Spin-up duration experiments indicate that Pearl River–derived sediment, which enters and accumulates in various regions of the model domain during the first year, continues to migrate southwestward in the second year under the influence of the mean annual flow field. In contrast, the spin-up duration of seabed sediment has little impact on the retentions of Pearl River–derived sediment on the shelf. Overall, this study reveals the transport pathway and fate of the Pearl River-derived sediment and provides a model-based assessment of its seasonal behavior and the sensitivity of suspended sediment dispersal to physical drivers and sediment parameters or conditions ~~dispersal mechanisms~~ on the northern SCS shelf. It identifies key physical

57 drivers regulating sediment transport and deposition patterns, offering new insight

58 into sediment fate in a monsoon-dominated shelf system.

59 **Keywords**

60 Riverine sediment transport; Sediment retention; Numerical modeling; Pearl River

61 Estuary

1. Introduction

63 The transport process of suspended sediment from river source to ocean sink is an

64 important link in the global material cycle (Geyer et al., 2004; McKee et al., 2004;

65 Kuehl et al., 2016; Liu et al., 2016; Cao et al., 2019). Much of the riverine sediment is

66 trapped on the shallow shoals in estuaries, while the rest is transported by buoyant

67 plume out of the estuary (Meade, 1969; Burchard et al., 2018; Zhang et al., 2019). The

68 riverine sediment carried by the buoyant plume has a significant impact on the water

69 quality, ecology, and geomorphology of the estuaries and continental shelves (Wright

70 and Coleman, 1973; Turner and Millward, 2002).

71 The transport and deposition of riverine sediments from river source to estuarine,

72 coastal, and shelf environments are controlled by diverse physical processes,

73 including tidal forces, wave action, and shelf circulation dynamics (Dalyander et al.,

74 2013; Gao and Collins, 2014; Xu et al., 2016; Warner et al., 2017; Zang et al., 2019;

75 Wang et al., 2020). Tides play a critical role in sediment transport dynamics in

76 estuarine and shelf regions, as spring tides typically produce higher bed shear stress,

77 enhanced sediment resuspension, and greater offshore sediment transport flux

78 compared to neap tides (Bever and MacWilliams, 2013; Zhang et al., 2019; Wang et

79 al., 2020). In nearshore regions, wave-induced bed shear stress often exceeds

80 current-induced stress by an order of magnitude (Xue et al., 2012; Dalyander et al.,

81 2013). Furthermore, wave-driven sediment resuspension frequently surpasses, and is

82 often several times greater than, the peak levels achieved by current-induced

83 resuspension (Sanford, 1994; Harris et al., 2008; Brand et al., 2010; Xu et al., 2016).

84 In shelf regions, circulation patterns significantly modulate sediment transport, with

85 the magnitude of along-shelf transport substantially exceeding the cross-shelf

86 component in most areas (Nittrouer and Wright, 1994; Geyer et al., 2004; Gao and

87 Collins, 2014; Wang et al., 2020).

88   Furthermore, sediment properties, including settling velocity (Xia et al., 2004;

89 Chen et al., 2010; Cheng et al., 2013), critical shear stress for erosion (Dong et al.,

90 2020), and bed grain size distribution (Xue et al., 2012; Bever and MacWilliams,

91 2013), significantly influence sediment transport dynamics and

92 deposition/resuspension processes. Settling velocity can influence the location of

93 sediment depocenters, with higher settling velocities leading to more proximal

94 entrapment and vice versa (Ralston and Geyer, 2017). Similarly, critical shear stress

95 for erosion can affect the resuspension of deposited sediment, with higher critical

96 shear stress resulting in less resuspension and more deposition especially during neap

97 tides and weak wind wave periods (Dong et al., 2020; Choi et al., 2023).

98   A comprehensive understanding of sediment transport and deposition from river

99 source to ocean sink requires the integrated consideration of both physical forcing

100 factors and inherent sediment characteristics. Here, we present the transport and

deposition of the Pearl River-derived sediments on the continental shelf as a case

study. The Pearl River, ranking as China's second-largest river in terms of freshwater

discharge (Hu et al., 2011), forms the Pearl River Estuary (PRE) in its lower reaches

(Figures 1 and S1). Its freshwater and sediment discharge are primarily delivered

through eight major outlets (Figure S1b; Wu et al., 2016; Zhang et al., 2019; Zhang et

al., 2025), forming distinct buoyant plumes that extend across the northern South

China Sea (SCS) shelf (Zhang et al., 2025). The present average annual (2001-2022)

freshwater and riverine sediment loads are 2.74×10^{11} m^3 and 2.84×10^7 tons,

respectively, as reported by the Ministry of Water Resources of the People's Republic

of China (Ministry of Water Resources of the PRC,

2022http://www.mwr.gov.cn/sj/#tjgb). The distribution of these inputs shows

significant seasonal variability: approximately 80% of the freshwater and 95% of the

sediment load are transported during the wet summer season (April to September),

while the remaining portion is discharged during the dry winter season (Xia et al.,

2004).

The northern SCS, under the influence ofshaped by the East Asian Monsoon,

displays marked seasonal contrasts, featuring winter monsoon winds averaging 7-10

m s^{-1} and summer winds typically below 6 m s^{-1} (Su, 2004; Ou et al., 2009). This

seasonal shift drives coastal currents: northeastward in summer and southwestward in

winter (Gan et al., 2009; Gan et al., 2013). Beyond the coastal zone, the consistent

SCS Warm Current (SCSWC) flows northeastward along the shelf break and inner

continental slope toward the Taiwan Strait, originating near Hainan Island and

persisting year-round, even during the winter northeast monsoon, across a remarkable distance of 600-700 km to the southern tip of the Taiwan Strait (Su, 2004; Yang et al., 2008).

The PRE is situated in the central part of the northern South China Sea boundary, positioned between the Taiwan Banks and Hainan Island. The PRE has a micro-tidal and mixed semi-diurnal regime~~,~~ with daily tidal inequality ~~in the range and in the time between the high and low tides~~ (Mao et al., 2004). The ~~neap and spring tides alternately influence the water elevation downstream of the estuary, with~~ tidal ranges vary~~ing~~ from approximately 0.7 m during neap tides to over 2 m during spring tides (Chen et al., 2016; Gong et al., 2018b). ~~The PRE and the nearby shelf exhibit strong seasonal variation in w~~Water column stratification is strong~~stability and are highly stratified~~ during the wet summer ~~season,~~ but weakens in the dry winter when ~~while~~ the PRE becomes partially mixed or vertically well-mixed ~~during the dry winter season~~ (Dong et al., 2004). Offshore ~~of the PRE region,~~ wave conditions are seasonally variable, being ~~display distinct seasonal patterns: the waves are~~ mild ~~during~~ in summer~~,~~ and ~~become~~ stronger ~~during~~ in winter, dominated ~~marked~~ by larger southeasterly waves (Gong et al., 2018a; Gong et al., 2018b; Zhang et al., 2021).

Previous studies have focused on sediment transport within the PRE (Zhang et al., 2019; Zhang et al., 2021; Ma et al., 2024). Most Pearl River-derived sediments are deposited within the estuary, and neglecting tidal effects can lead to higher deposition rates and lower offshore sediment flux when compared to those with tides (Hu et al., 2011). Pearl River-derived sediment behavior ~~The depositional dynamics of sediments~~

from different PRE outlets ~~are~~ is regulated by outlet location, topography, and tidal phase~~conditions~~, with neap tides favoring sediment accumulation on shoals and spring tides driving erosion and enhancing erosion and export~~offshore sediment transport~~ (Zhang et al., 2019). Waves further intensify both lateral trapping within the PRE and offshore sediment transport (Liu and Cai, 2019; Zhang et al., 2021).

However, numerical studies on the transport of the Pearl River-derived sediments across the continental shelf remain scarce, even amidst the widespread adoption of computer modeling approaches. Previous research ~~on the distribution of these sediments~~ has primarily relied on analyses of seismic profiles, gravity cores, and laboratory-based radiometric dating of sediment samples (Ge et al., 2014; Liu et al., 2014; Cao et al., 2019; Lin et al., 2020; Chen et al., 2023). Outside the PRE, ~~gravity core and seismic survey~~such data ~~were used to examine the Holocene sedimentary processes,~~ reveal~~ing~~ two Holocene ~~distinct~~ mud depo-centers: an eastward proximal depo-center extending southeastward from the PRE's mouth and a southwestward distal mud belt (Ge et al., 2014; Liu et al., 2014; Chen et al., 2023). However, seismic and drilling data cannot confirm transport of ~~that the~~ Pearl River sediment~~s~~ ~~can be transported~~ to the Beibu Gulf (Ge et al., 2014), and limited sampling makes it ~~Due to the lack of sufficient gravity core samples and seismic data, it is~~ difficult to quantify their contribution~~quantitatively attribute the sediment in the Beibu Gulf to the Pearl River-derived sediment~~ (Cao et al., 2019). Using radionuclide endmember models~~Afterward~~, Lin et al. (2020) estimated that ~15% of nearshore surface sediments in the Beibu Gulf originate from the PRE, but their study did not address

transport pathways, fluxes, or annual deposition. ~~used the ^{226}Ra — ^{238}U and ^{232}Th — ^{238}U endmembers model based on measurements of radionuclides in the surface sediment samples. They found that approximately 15% of the surface sediment in the nearshore area of the Beibu Gulf originates from the PRE region. However, their studies only address the proportion of the PRE sediment in the surface sediment of the Beibu Gulf, without directly indicating the seasonal transport pathways, flux, and annual deposition of the sediment from the Pearl River.~~

A gap persists in understanding how physical drivers ~~processes~~ (such as tides, waves, and remotely forced (large-scale, non-local forcing) ambient shelf circulations) and sediment characteristics (such as critical shear stress for erosion, settling velocity) and sediment initial conditions influence the seasonal suspension, transport, and annual deposition of the Pearl River-derived sediment on the shelf. ~~Specifically, this study focuses on sediment classes 4 and 5 in Table 1, which represent the Pearl River-derived components: slow-settling single fine grains (Class 4) and fast-settling flocs (Class 5), in contrast to the background seabed sediments represented by classes 1 to 3.~~ To address this, we utilize numerical modeling calibrated and validated with field observations and seabed grain size data, ~~complemented by extensive collection of field observations and seabed grain size distribution data for model calibration and validation — a highly effective approach for exploring mechanisms and testing hypotheses derived from limited observational datasets~~. This is an effective approach for investigating processes and testing hypotheses where observations are limited. This study ~~aims to~~ systematically examines ~~investigate~~ the dispersal dynamics of ~~the~~

Pearl River-derived sediment ~~over~~ on the northern South China Sea shelf, focusing~~with particular emphasis~~ on the following objectives:

(1) Quantify the seasonal dispersal and annual deposition of ~~the~~ Pearl River-derived sediment ~~(classes 4 and 5 in Table 1)~~ on ~~over~~ the continental shelf.

(2) Examine the relative roles of physical forcings (tides, waves, and ambient circulations), sediment characteristics (critical shear stress for erosion, settling velocity) and (Pearl River-derived versus Seabed) sediment spin-up durations on its ~~the~~ dispersal ~~of the Pearl River-derived sediment~~.
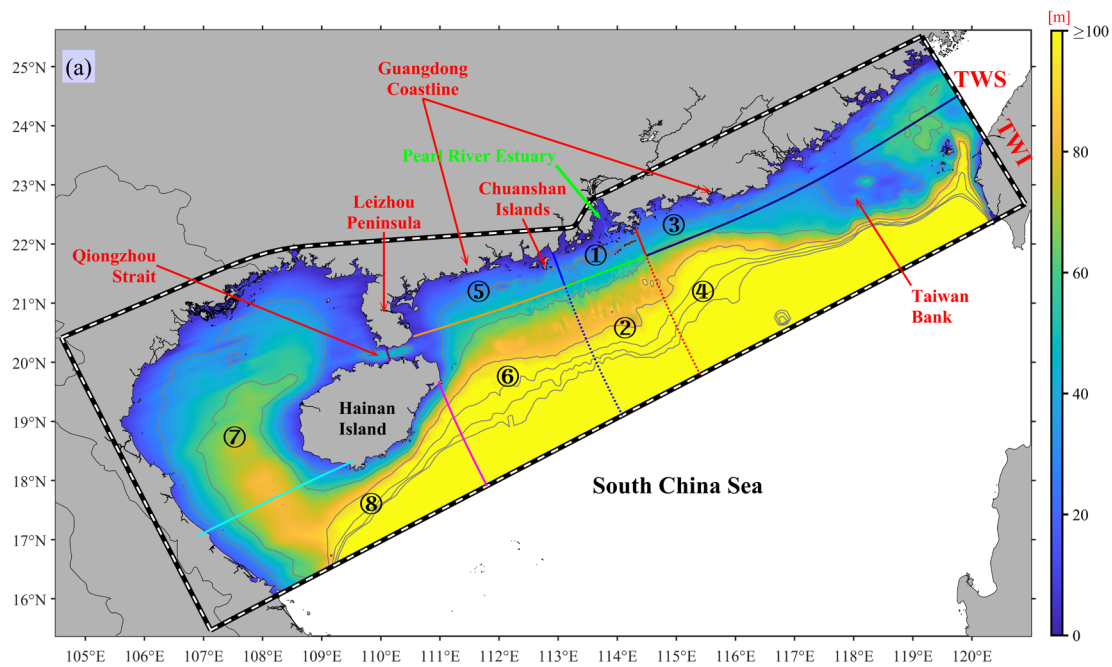
Figure 1. Bathymetry (shading) and isobath contours of the study area, with the ROMS/SWAN model grid domain outlined by black-to-white dashed lines. Circled numbers ① - ⑧ denote the eight regions: "Proximal", "Southern", "Eastern", "Southeastern", "Western", "Southwestern", "Gulf", and "Distal" regions, as defined

203 by transects and detailed in Section 2.1. The abbreviations TWI and TWS mean

204 Taiwan Island and Taiwan Strait, respectively. The gray contours represent 30-180 m

205 isobaths at 30 m intervals, a consistent feature maintained in all subsequent figures

206 that include these isobath contours.

207

208 2. Methods

209 2.1 Model coupling

210   This study employed the Coupled Ocean Atmosphere Wave Sediment Transport

211 (COAWST, version 3.4) modeling system (Warner et al., 2005; Warner et al., 2008;

212 Warner et al., 2010), which includes a Model Coupling Toolkit (MCT) to facilitate

213 data exchange among different modules (Jacob et al., 2005; Larson et al., 2005). The

214 COAWST system consists of several modeling components, mainly comprises a

215 hydrodynamic module (Regional Ocean Modeling System; ROMS) (Shchepetkin and

216 McWilliams, 2005; Haidvogel et al., 2008), an atmospheric module (Advanced

217 Research Weather Research and Forecasting; WRF) (Skamarock et al., 2005), a wave

218 module (Simulating Waves Nearshore; SWAN) (Booij et al., 1999), and a sediment

219 transport module (Community Sediment Transport Modeling System; CSTM)

220 (Warner et al., 2008).

221   In this study, we established a coupling between ROMS, SWAN, and CSTM. The

222 model grid covered the northern continental shelf of the South China Sea, including

223 the PRE (Figure 1). The regional model was configured with 170×482 horizontal

224 grid cells, with horizontal resolution varying from approximately 0.1 km near the PRE

225 to about 10 km at outer open boundaries (Hu et al., 2024; Zhang et al., 2025). The

226 model grid bathymetry data was obtained from nautical charts compiled by the China

227 Maritime Safety Administration and the General Bathymetric Chart of the Oceans

228 (GEBCO) (Weatherall et al., 2015). The vertical grid used a terrain-following

229 S-coordinate system (Song and Haidvogel, 1994) with 20 layers and a stretching

230 transformation for higher resolution near the surface and bottom. For model

231 validations, please refer to the Supplementary Material (Supplement Figures S1-S10).

232   To improve the understanding of the spatial-temporal variabilities in the riverine

233 sediment dispersal, and the estimation of the fate of the Pearl River sediment during

234 the wet summer season, dry winter season, and throughout the year, we partitioned the

235 model domain into eight distinct regions delineated by various transects as illustrated

236 in Figure 1. The division criteria are mainly based on the distance from the estuary

237 and the natural separation by the Leizhou Peninsula and Hainan Island (Figure 1).

238 These regions include:

239   ① Proximal region: Proximity to the estuary,

240   ② Southern region: Located deeper in the southern part of the estuary,

241   ③ Eastern region: Eastern side of the estuary, closer to the shoreline,

242   ④ Southeastern region: Further offshore on the eastern side of the estuary,

243   ⑤ Western region: Western side of the estuary, closer to the shoreline,

244   ⑥ Southwestern region: Offshore on the western side of the estuary,

245   ⑦ Gulf region: Mainly the Beibu Gulf,

246   ⑧ Distal region: South of the Hainan Island.

247   By dividing the model domain into these delineated regions, we calculated the

248   riverine sediment flux for each transect, thereby determining the total riverine

249   sediment volume retained in each region.

250   **2.2 ROMS model setup**

251   For the ROMS model, we utilized the Generic Length Scale turbulence closure

252   scheme (Warner et al., 2005) for vertical turbulence parameterization. The method of

253   Smagorinsky (1963) was employed to calculate the horizontal eddy viscosity and

254   diffusivity. The Flather and Chapman boundary conditions were applied to barotropic

255   current and water elevation at open boundaries, respectively (Flather, 1976; Chapman,

256   1985). Meanwhile, the open-boundary conditions for temperature, salinity, and

257   sediment concentration were imposed by radiation methods (Orlanski, 1976;

258   Raymond and Kuo, 1984). Surface forcing (including wind, net shortwave radiation,

259   air temperature, atmospheric pressure, specific/relative humidity, and rain, etc.) data

260   were sourced from the Climate Forecast System Reanalysis of the National Centers

261   for Environmental Prediction (NCEP) (Saha et al., 2014), with a temporal resolution

262   of 1 h and a spatial resolution of 0.3° × 0.3°. Water level and current velocity

263   open-boundary conditions comprised two components: tidal and subtidal. The tidal

264   component was obtained from the Oregon State University Tidal Prediction Software

265   database (Egbert and Erofeeva, 2002), while the subtidal component was interpolated

266   from the HYbrid Coordinate Ocean Model (HYCOM) outputs (Chassignet et al.,

267   2007).

268   **2.3 Wave model setup**

269   The SWAN model was executed and coupled to the same grid as the ROMS

270   model (Warner et al., 2010). It was driven by surface atmospheric forces, real-time

271   water level, and current fields from the ROMS and boundary reanalysis data. Wave

272   boundary conditions were specified using nonstationary wave parameters from

273   outputs of the NOAA WAVEWATCH III global ocean wave model solutions (Tolman

274   et al., 2016). Information was exchanged at 15-minute intervals to introduce

275   wave-current interaction (WCI) between the ROMS and SWAN models (McWilliams

276   et al., 2004; Kumar et al., 2012). This exchange included significant wave height

277   (Hsig), surface peak wave period, mean wave direction and length, wave energy

278   dissipation, and the percentage of breaking waves from SWAN to ROMS, as well as

279   water level and current from ROMS to SWAN.

280   Additionally, the wave-current bottom boundary module based on Madsen (1994),

281   was activated to simulate the wave-current bottom boundary layer. The vortex force

282   module of wave forces was also activated to compute the wave-induced momentum

283   flux, utilizing the method proposed by McWilliams et al. (2004) and implemented in

284   COAWST by Kumar et al. (2012). The bottom friction was computed based on a

285   logarithmic velocity profile (Warner et al., 2008).

286   **2.4 Specifications of riverine input and sediment model**

287   The freshwater discharge for the Pearl River was specified at the northern

288   boundary using daily measured data from the Pearl River Water Resources

289   Commission, while downstream precipitation within the Pearl River Basin was

290   neglected. The full simulation model was initialized on the first day of January 2016

using temperature, salinity, and current fields interpolated from the HYCOM model, and it concluded on March 31, 2018. This study primarily analyzes the last 12 months, specifically from April 1, 2017, to March 31, 2018. This year was selected because the freshwater discharge and sediment load of the Pearl River closely approximated the average values of the past two decades, with a runoff of 3.35×10^{11} m^3 and a sediment load of 3.45×10^7 tons, closely resembling the averages from 2001 to 2022.

Since the daily riverine sediment loads were unavailable, we modified the previous research results on sediment rating curves (Zhang et al., 2012) to suit for our study, as expressed by

$$C\_s = 0.00002263Q^{1.792} \tag{1}$$

where C_s is the Pearl River-derived suspended sediment concentration (mg L^{-1}), Q is the Pearl River freshwater discharge rate (m^3 s^{-1}). Based on this relationship, the total amount of Pearl River sediment input over our 12-months study period (Figure 3b) was 34.52 million tons, aligning closely with the annual load reported in 2017 by the Pearl River Water Resources Commission. The riverine sediment input, derived from the river discharge, was allocated across the eight outlets along the north boundary (Figure S1b) based on the distribution approach of Hu et al. (2011). The subsequent step involved establishing the proportion of seabed sediment particle size components. Sediments are typically categorized into three grain-size classes: clay (0-4 μm), silt (4-63 μm), and sand (63-2000 μm), as outlined by Shepard (1954). Data on sediment particle size composition for the northern continental shelf of the South China Sea and the PRE area were acquired through multiple voyage observations

313 ([Zhang et al., 2013](); [Zhang et al., 2019]()). Furthermore, publicly available data from

314 published literature were compiled ([Gao et al., 2007](); [Kirby et al., 2008](); [Gao et al.,]()

315 [2010](); [Huang et al., 2013](); [Liu et al., 2014](); [Wang et al., 2014](); [Wang et al., 2015](); [Wang]()

316 [et al., 2016](); [Ge et al., 2017](); [Lu et al., 2017](); [Zhong et al., 2017](); [Yang et al., 2018](); [Ge]()

317 [et al., 2019]()). Finally, component distribution data for different particle size classes of

318 seabed sediment were obtained from a total of 1,981 measured stations (Figure 2a-c).

319

320
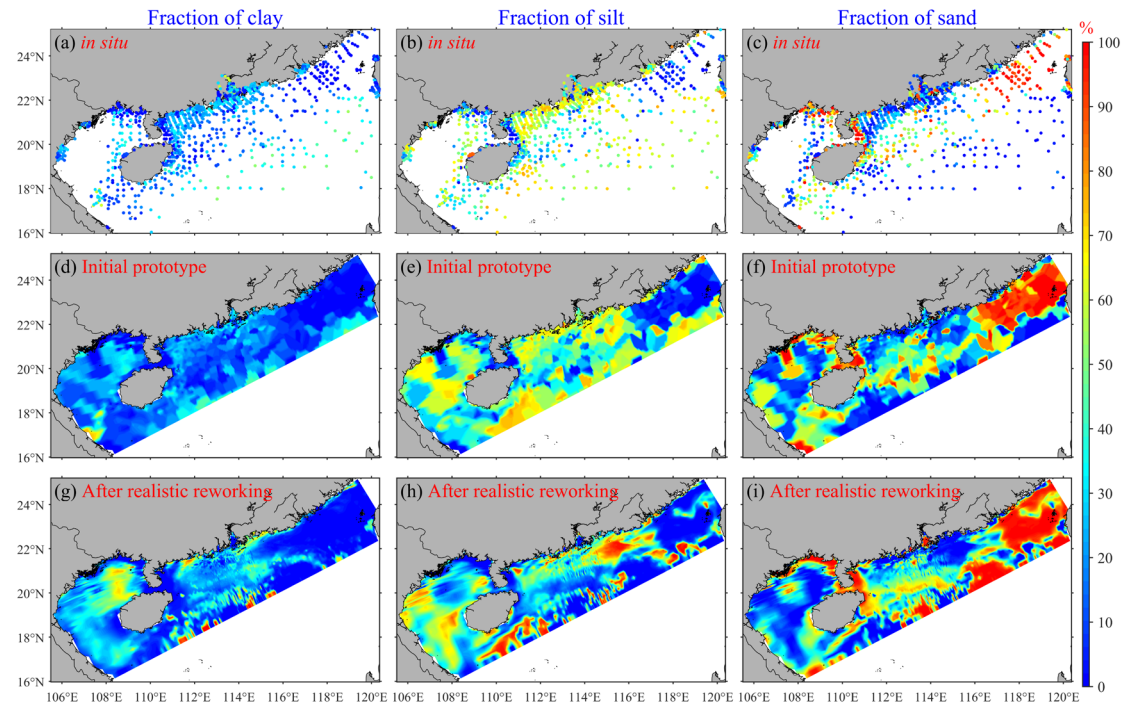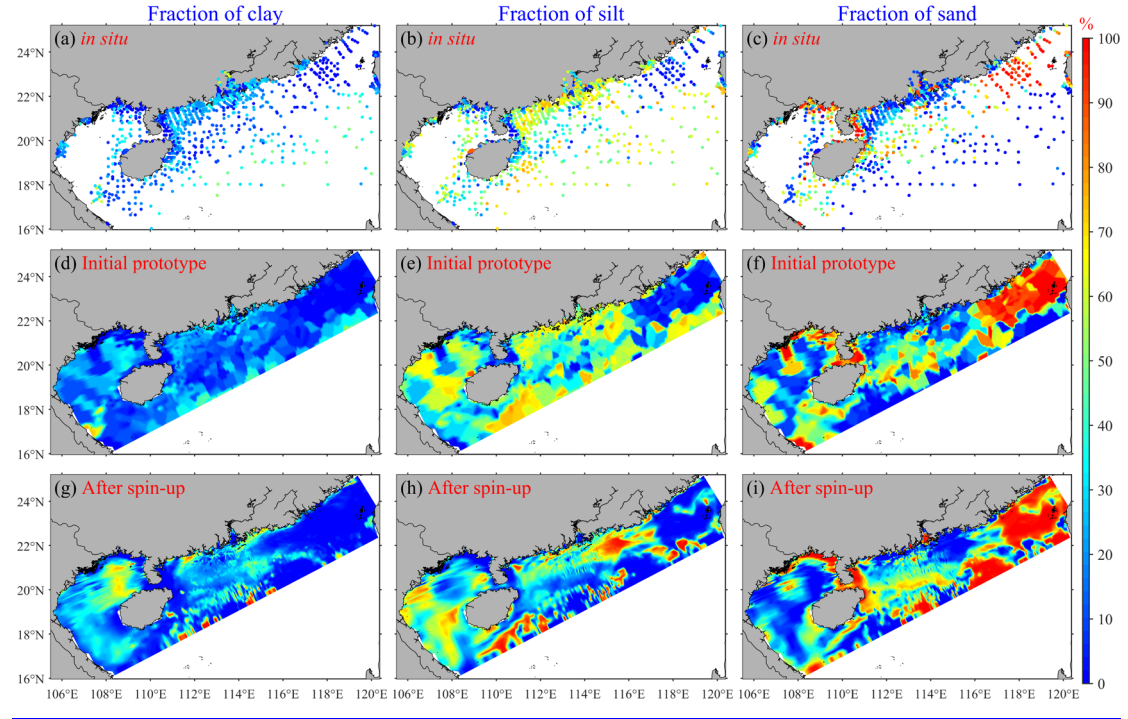
Figure 2. Row 1 presents the spatial distribution patterns of seabed sediment fractions derived from 1,981 sampling sites, while Row 2 demonstrates the initial spatial distribution prototype of seabed sediment fractions developed based on the observational data presented in Row 1. Row 3 shows the spatial distribution patterns of seabed sediment fractions following the completion of spin-up phase in the Control run case on April 1st, 2017, with Columns 1, 2, and 3 representing the fractions of clay, silt, and sand, respectively.

As illustrated in Figure 2a-c, the measured stations exhibit a widespread distribution, offering comprehensive coverage of the entire northern continental shelf of the South China Sea, including the PRE. Particularly dense distribution is observed in the PRE and the coastal areas of western Guangdong. These regions represent the primary scope of transport and deposition associated with the Pearl River-derived

335 sediment. Hence, the stations utilized in this study well represent the distribution of

336 bed sediment particle size components in these study areas. It is evident that among

337 the stations in the offshore area of the northern continental shelf of the South China

338 Sea, silt dominates, followed by clay, while sand with the largest particle size is the

339 least abundant. This suggests a significant presence of terrestrial sediment or Pearl

340 River sediment in the offshore area of the northern continental shelf of the South

341 China Sea. It should be noted that the lack of in situ grain size distribution data in

342 specific regions of the model domain, especially in the Beibu Gulf area, may lead to

343 uncertainties in sediment transport predictions. We will address these limitations and

344 quantify their potential errors in the discussion part of this study.

345 To derive the component proportions of the initial prototype field on the model

346 grid, this study employed the Kriging method (Krige, 1951), widely recognized for

347 spatially interpolating various types of observational data. The sediment distribution

348 pattern obtained through interpolation (Figure 2d-f) closely resembles the original

349 1,981 measured sediment particle size distribution patterns (Figure 2a-c), suggesting

350 the suitability of this interpolation method for the study area.

351 The initial prototype field underwent a 15-month spin-up period (from January 1,

352 2016, to March 31, 2017), during which the bottom sediment composition evolved in

353 response to under realistic hydrodynamic forcings through from the coupled ROMS,

354 SWAN, and CSTM models. This method has been utilized in numerous previous

355 studies, including those by Bever et al. (2009), van der Wegen et al. (2010), and

356 Zhang et al. (2021). This process allows the initially estimated idealized sediment

357 distribution to evolve under ~~realistic dynamic forcings, including~~ tides, waves, and

358 currents, thereby minimizing unreasonable spatial patterns introduced by the Kriging,

359 sparse or problematic data ~~interpolation method~~. Such unreasonable spatial patterns

360 may arise due to limitations in the number, representativeness, and timing of field

361 sediment samples relative to the model start date. As a result, the sediment field after

362 the spin-up period (Figures 2g–i) is thought to exhibit~~s~~ spatial patterns that are ~~more~~

363 ~~physically plausible and~~ better aligned with the hydrodynamic conditions of the study

364 region. During both the 15-month spin-up period and the subsequent 12-month formal

365 model experiments (see Section 2.6 and Table 2), the CSTM utilized five sediment

366 classes (Table 1), representing a range of sediment sizes and characteristics. These

367 included three types of seabed sediments (clay, silt, and sand, corresponding to

368 sediment Classes 1 to 3 in Table 1) and two types of Pearl River-derived sediments

369 (Class 4 and Class 5 in Table 1). The riverine sediments consisted of slow-settling

370 single fine grains (Class 4) and high-settling flocs (Class 5), which were delivered

371 into the model domain during both the 15-month spin-up period and the subsequent

372 12-month formal model experiments. The riverine flocs correspond to the flocculated

373 fractions of clay and silt, whereas the single fine grains represent the non-flocculated

374 components within the Pearl River-derived sediments, following the setting of Bever

375 and MacWilliams (2013). To clarify, at the start of the 12-month formal model

376 experiments, the retained Pearl River-derived sediments (Classes 4-5 in Table 1) that

377 entered the model during the 15-month spin-up period were added ~~as~~ to Class 1 and

378 Class 2, respectively, to avoid contaminating the data analysis of the formal

experiments. This approach allows for a better distinction between Pearl River sediment and seabed sediment, enabling separate analysis of the suspension, transport, and deposition of Pearl River-derived sediment (Harris et al., 2008; Zhang et al., 2019). Specifically, the fractions of the two types of Pearl River-derived sediments were set at 40% and 60%, respectively, following Zhang et al. (2019) and Zhang et al. (2021). The parameters for all five sediment classes are summarized in Table 1. Sediment density, porosity, and erosion rate for all sediment classes were set to 2650 kg m^{-3}, 0.672 (Zhang et al., 2019; Zhang et al., 2021), and 1×10^{-4} kg m^{-2} s^{-1} (Ralston et al., 2012), respectively. Settling velocities (w_s) were guided by the ranges reported by Xia et al. (2004) and Warner et al. (2017), and further refined through extensive sensitivity testing and model calibration to optimally reproduce observed suspended sediment concentration (SSC). ~~The settling velocity (w_s), c~~Critical shear stresses for erosion (τ_{ce}), and other parameters were set following previous studies or were based on model calibration (Ralston et al., 2012; Warner et al., 2017; Zhang et al., 2019; Dong et al., 2020; Zhang et al., 2021; Cao et al., 2025).

Our model configuration incorporates seasonal variations in τ_{ce}, supported by multiple lines of evidence from field observations, laboratory experiments, and numerical analyses (Dong et al., 2020; Cao et al., 2025). Previous studies have established a distinct seasonal pattern in the PRE, with winter τ_{ce} values significantly exceeding those in summer. Dong et al. (2020)'s laboratory experiments using the UMCES-Gust Erosion Microcosm System (U-GEMS) on 2017-winter sediment samples yielded a τ_{ce} of 0.26 Pa, which effectively reproduced observed ~~suspended~~

sediment concentration (SSC) in winter simulations. However, this value proved excessive for summer conditions, when a τ_{ce} of 0.15 Pa provided better agreement with field observations in summer simulations, indicating a winter-to-summer τ_{ce} ratio of 1.73. Recent 2020-summer in situ measurements by Cao et al. (2025) using a benthic quadrapod-mounted 3D Profiling Sonar revealed a two-layer erosion threshold system: a surface "fluffy layer" with τ_{ce} = 0.06 Pa overlying a consolidated seabed with τ_{ce} = 0.13 Pa. The latter value aligns with Dong et al. (2020)'s summer calibration, suggesting that Dong et al. (2020)'s laboratory measurements, potentially affected by sediment consolidation during sample transport, might have missed the lower τ_{ce} of the surface fluffy layer. Based on these consistent findings, we implemented a seasonal τ_{ce} adjustment factor of 1.73 (winter/summer) in our model configuration (Table 1).

Table 1. CSTM model Sediment Properties

Source	Seabed			Pearl River	
Class	1	2	3	4	5
Sediment Type	Clay	Silt	Sand	Single grains	Flocs
w_s (mm s^{-1})	0.02[c]	1.2[c]	57[d]	0.005[c]	0.6[c]
Summer τ_{ce} (Pa)	0.14[e]	0.03	0.27[d]	0.15[abef]	0.05[abe]
Winter τ_{ce} (Pa)	0.24[f]	0.05[f]	0.47[df]	0.26[abf]	0.09[abf]
Fraction	Spatially variable, see Figure 2g-i			40%[ab]	60%[ab]

[a]Zhang et al. (2019), [b]Zhang et al. (2021), [c]Calibrated, [d]Warner et al. (2017), [e]Cao et al. (2025), and

416 [f](Dong et al., 2020).

417

2.5 Wet and dry season regimes

419 The study area exhibits pronounced seasonal variability, which can be distinctly

420 categorized into two primary seasons (Dong et al., 2004; Su, 2004; Liu et al., 2014;

421 Zhang et al., 2021). This seasonal classification is supported by multiple

422 environmental parameters, including river freshwater discharge (Figure 3a), riverine

423 sediment load (Figure 3a), wind patterns (Figure 3b), air temperature (Figure 3c), and

424 modeled wave conditions (Figure 3d-f) at a representative site (21.5°N, 114°E;

425 corresponding to station W1 in Figure S1a, located immediately south of the PRE).

426 All values presented in Figure 3 correspond to the period from April 1, 2017, to

427 March 31, 2018, consistent with the 1-year model simulation. The daily measured

428 freshwater discharge for the Pearl River was obtained from the Pearl River Water

429 Resources Commission, while the riverine sediment load was estimated using the

430 method described in Section 2.4. The meteorological data for wind and air

431 temperature were obtained from the NCEP reanalysis dataset, while wave parameters

432 were derived from numerical model simulations. These comprehensive indicators

433 collectively characterize the distinct seasonal patterns observed in the study area

434 (Figure 3). The entire year (from April 1, 2017, to March 31, 2018) is typically

435 divided into two main seasons: wet summer (from April 1, 2017, to September 30,

436 2017) and dry winter (from October 1, 2017, to March 31, 2018).

437 During the wet summer season, freshwater discharge tends to be notably high,

438 often exceeding 10,000 m^3 s^{-1} and reaching a maximum of 53,000 m^3 s^{-1}, with an

439 average value of 15,266 m^3 s^{-1}. This discharge constitutes a significant portion of the

440 entire year, accounting for 72.06% of the annual total. During this period, the river

441 carries a substantial sediment load of 32.85 megatons, constituting 95.17% of the total

442 annual sediment transport. Prevailing winds predominantly blow from the south. For

443 example, Figure 3b depicts the average monthly wind vector direction during the

444 summer months as northward, with weak southeasterly winds in April, May, and

445 September, and moderate southeasterly winds in July. June and August experience

446 moderate southwesterly winds. The 2 m height air temperatures typically range

447 between 20℃ and 30℃. The daily average Hsig remains relatively low, with the

448 monthly average Hsig less than 1 m. The wave propagation direction is generally

449 consistent with the wind direction, being easterly in April and May, and southerly

450 from June to September.

451   In stark contrast, the dry winter season demonstrates markedly lower runoff,

452 typically falling below 10,000 m^3 s^{-1}, with an average value of 5,953 m^3 s^{-1}. The

453 sediment load during this period is significantly reduced to merely 1.67 megatons,

454 marking a substantial decrease compared to the wet summer season. Prevailing winds

455 during the dry winter are predominantly northeasterly, with relatively high wind

456 speeds. Except for moderate wind intensity in March, the monthly average wind speed

457 in other months exceeds 5 m s^{-1}. The 2 m height air temperatures typically range

458 between 10℃ and 25℃ during this season. The wave propagation direction aligns

459 with the prevailing northeasterly winds of the season, predominantly northeasterly.

460

461
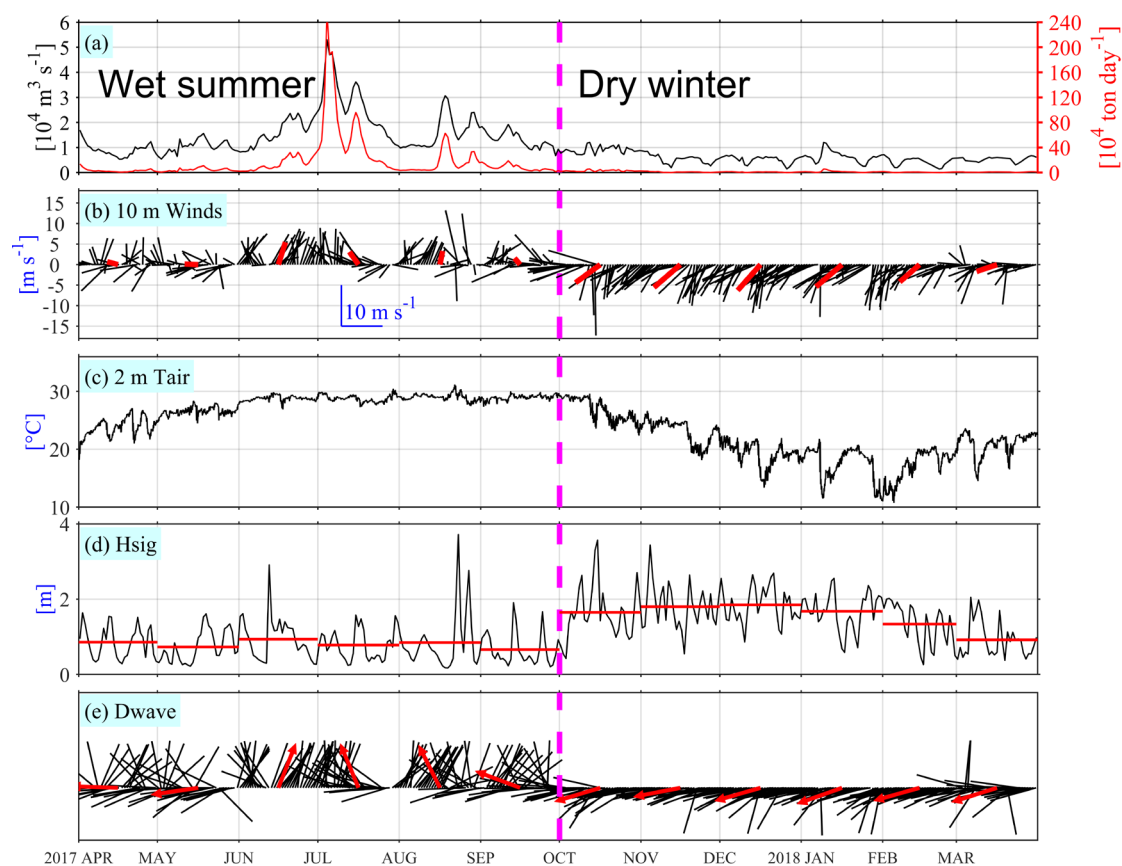
Figure 3. Time series of (a) the daily Pearl River freshwater discharge and sediment

load, (b) daily (black vectors) and monthly (red vectors) averaged 10-meter height

winds, (c) hourly 2-meter height air temperature, daily (black) and monthly (red)

averaged (d) significant wave height (Hsig, lines) and (f) wave propagation direction

(vectors) weighted by $Hsig^2$. Two distinct seasons are delineated by the dashed

magenta line.

468

2.6 Model experiments

To assess the relative importance of tides, waves, ambient shelf currents and

residual water levels, seasonal variation in critical shear stress for erosion, the settling

472 velocity, and the spin-up duration of Pearl River-derived sediment (Classes 4-5 in

473 Table 1) in the transport and dispersal of Pearl River-derived sediments, we conducted

474 seven simulation experiments (Table 2). In all experiments, we implemented the

475 Charnock approach within COAWST's bulk air-sea flux parameterization scheme to

476 calculate surface wind stress using the NCEP 10-m wind product (Charnock, 1955;

477 Fairall et al., 1996), ensuring consistency in wind stress forcing across all simulations.

478   Exp 1 (the **Control** run) incorporated all the aforementioned forcing agents

479 (including winds) and accounted for the seasonal variation in critical shear stress for

480 erosion, with the winter critical shear stress for erosion set to be 1.73 times of that in

481 summer. Exp 2 (**NTS** hereafter) was identical to Exp 1 but excluded tides, while Exp

482 3 (**NWS** hereafter) excluded waves. In Exp 4 (**NAS** hereafter), waves, tides, and the

483 seasonal variation in critical shear stress for erosion were included, but the remotely

484 forced (large-scale, non-local forcing) ambient shelf current and residual (non-tidal)

485 water levels were omitted (i.e., no subtidal circulation forcing at open boundaries) to

486 examine the influence of the South China Sea circulation. Exp 5 (NVS hereafter)

487 replicated the setup of Experiment 1, but with one modification: it used a constant

488 critical shear stress for erosion (τ_{ce}) across both seasons, specifically adopting the

489 summer τ_{ce} value from Table 1 throughout the simulation (i.e., no seasonal adjustment

490 between winter and summer). Exp 6 (**DSV** hereafter) was identical to Exp 1, except

491 that it set a double sediment settling velocity of the Exp 1. Finally, to assess the

492 model's sensitivity to the spin-up duration of Pearl River-derived sediment,

493 particularly regarding the retention of riverine sediments in both the water column and

the seabed, we adopted the sediment distributions (Classes 1 to 5) from the final state of the Control run on March 31, 2018, as the alternative initial conditions for the Cycle experiment (designated as Exp 7, **Cycle** hereafter). This setup carries over the full year's evolution of riverine sediment transport and deposition from the Control run (Exp 1), including changes in all sediment classes, into the start of Exp 7. As a result, Exp 7 mainly evaluates how the presence of previously deposited riverine sediments influences subsequent sediment transport estimates.

Table 2. Experiment Settings

Experiments	Tides	Waves	Ambients	τ_{ce}	w_s	Re-run
Exp 1 (Control)	✓	✓	✓	Variable	Original	✗
Exp 2 (NTS)	✗	✓	✓	Variable	Original	✗
Exp 3 (NWS)	✓	✗	✓	Variable	Original	✗
Exp 4 (NAS)	✓	✓	✗	Variable	Original	✗
Exp 5 (NVS)	✓	✓	✓	Constant	Original	✗
Exp 6 (DSV)	✓	✓	✓	Variable	Double	✗
Exp 7 (Cycle)	✓	✓	✓	Variable	Original	✓

The term 'Ambients' denotes remotely forced (large-scale, non-local forcing) ambient shelf currents and residual (non-tidal) water levels. Variable indicates simulations employing seasonally varying τ_{ce} values (from Table 1), while 'Constant' refers to runs using exclusively the summer τ_{ce} value throughout the entire experiment. 'Original'

507 designates cases utilizing the settling velocities specified in Table 1, whereas 'Double'

508 indicates simulations with these values doubled."

509

510 **3 Results**

511 **3.1 Seasonal hydrodynamics and transport patterns of the Pearl**

512 **River-derived sediment**

513   We quantified the spatial distributions of seasonal mean wind stress, Hsig, wave

514 bottom orbital velocity (WBOV), and bottom shear stress for both the wet summer

515 and dry winter periods (as defined in Section 2.5). These distributions serve as

516 representative hydrodynamic conditions for typical summer and winter scenarios,

517 respectively (Figure 4).

518   During summer, the prevailing winds predominantly originate from the south,

519 with the average wind stress generally below 0.03 Pa, except in the eastern coastal

520 waters of Hainan Island, where localized values reach up to 0.05 Pa (Figure 4a). In

521 contrast, during the dry winter season, the prevailing winds shift to a northeasterly

522 direction, resulting in generally higher average wind stress compared to summer

523 (Figure 4b), with values typically exceeding 0.1 Pa in areas deeper than 40 m and

524 surpassing 0.2 Pa in the offshore eastern Guangdong Coast near the Taiwan Bank (see

525 Figure 1).

526   Corresponding to the seasonal wind stress (Figures 4a-b), the seasonally averaged

527 wave characteristics in the PRE and the adjacent northern continental shelf of the

528 South China Sea exhibit significant seasonal variations (Figures 4c-d).

529   During the wet summer season, the Hsig in the studied area is relatively low, with

530   waves predominantly coming from the southeast (Figure 4c). The seasonal average

531   Hsig across the entire shelf remains below 1 m, with areas deeper than 60 m showing

532   Hsig values above 0.8 m, while in shallower nearshore regions (water depth < 20 m),

533   Hsig is less than 0.6 m (Figure 4c). Corresponding to the lower Hsig in the wet

534   summer, the seasonally-averaged WBOV is also relatively small, generally less than 1

535   cm s^{-1} in areas deeper than 40 m, except in some nearshore shallow water regions

536   where it reaches up to 10 cm s^{-1} (Figure 4e). The seasonally-averaged bottom shear

537   stress during the wet summer is relatively high in the PRE, nearshore regions, and the

538   Taiwan Bank, where tidal dissipation is strong (Figure 4g).

539   In the dry winter season, the Hsig increases significantly compared to the wet

540   summer, with waves primarily coming from the northeast, although refraction occurs

541   in some nearshore regions, changing the wave direction to southeasterly (Figure 4d).

542   The area with water depths exceeding 60 m has a Hsig greater than 1.5 m, while in the

543   20-meter depth region, the Hsig reaches approximately 1 m (Figure 4d). Compared to

544   the wet summer, the WBOV increases significantly in the PRE mouth and many

545   nearshore regions, reaching up to 10-20 cm s^{-1} (Figure 4d). The average bottom shear

546   stress on the continental shelf outside the estuary also increases significantly during

547   the dry winter compared to the wet summer (Figure 4f).

548

549
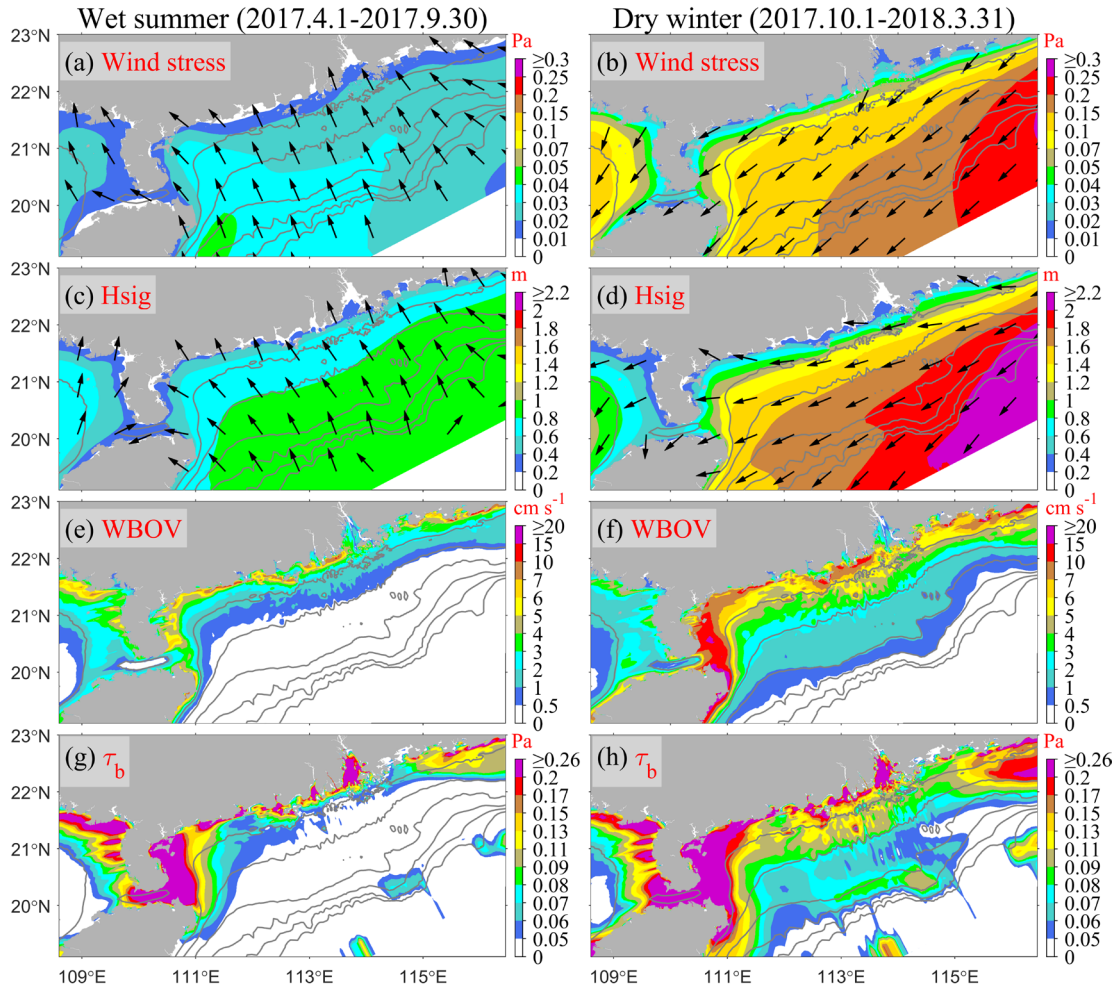
Figure 4. The patterns of variables averaged for the wet summer season (April 1st to

September 30th, 2017; Column 1) and the dry winter season (October 1st to March

31st, 2018; Column 2) in the Control case. Row 1 (a-b) depicts wind stress (color) and

direction (vectors), Row 2 (c-d) shows Hsig (color) and propagation direction (vectors)

weighted by Hsig², Row 3 (e-f) presents wave bottom orbital velocity (WBOV), and

Row 4 (g-h) displays bottom shear stress magnitude.

556

557   The patterns of residual sediment dispersal, flux, and deposition over the

558   simulation period provide clear information on the mechanisms for sediment

559   redistribution on both annual and seasonal timescales. The following section presents

560   a detailed analysis of the seasonally averaged fields of salinity, flow, riverine SSC,

561   depth-integrated riverine sediment flux, and riverine sediment deposition patterns

562   during the wet summer season (Figure 5) and dry winter season (Figure 6) on the

563   continental shelf.

564   During the wet summer season, when freshwater discharge is high and water

565   column stratification is strong, riverine SSC ("riverine" means only Pearl

566   River-derived sediment, classes 4-5 in Table 1, as follows) is primarily influenced by

567   advection from the buoyant river plume (salinity less than 33.5 in Figure 3a, as

568   follows) into the shelf sea, primarily in the surface layer (Figures 5a-b), high SSC

569   regions closely align with the buoyant plume, as sediment is efficiently transported by

570   the low-salinity, high-momentum freshwater outflow (Figures 5a-d). The buoyant

571   plume extends both northeastward and southwestward along the coastline (Figure 5a).

572   Due to the influence of southerly winds (Figure 4a) and ambient shelf currents, the

573   extent of the buoyant plume extending northeastward is significantly higher than that

574   extending southwestward. In terms of riverine sediment suspension, its estuarine

575   turbidity maxima (ETM) zone (~100 mg L^{-1}) is situated in the shallow water area

576   within the estuary (water depth < 10 m) (Figure 5c-d). Beyond the estuary, suspended

577   riverine sediment disperses across the shelf through the buoyant plume. Further away

578   from the estuary, its distribution aligns with that of the buoyant plume, with

579   concentrations diminishing as dispersal distance increases. The depth-integrated

580   advective horizontal flux (without including vertical processes such as settling,

581   resuspension, or diffusion, which are handled separately within the model) of riverine

582   sediment offers a clear indication of the primary net transport pathway of the riverine

583   sediment (Figure 5e). The riverine sediment exhibits both southwestward and

584   northeastward fluxes (Figure 5e). Southwestward coastal transport can extend as far

585   as the Leizhou Peninsula and Hainan Island. On the eastern side, the northeastward

586   transport extends toward the Taiwan Bank. However, the primary transport pathway

587   there is diverted southward (Figure 5e) due to the obstruction caused by summer

588   upwelling near the Guangdong east coast (Chen et al., 2017a; Chen et al., 2017b), as

589   evidenced by the cross-shore current in the bottom layer (Figure 5b). The

590   southwestward transport pathway follows the region where the water depth is

591   shallower than 30 m, with a riverine sediment flux of 10–20 g m^{-1} s^{-1}. In contrast, the

592   northeastward transport pathway occurs in the 30–60 m depth range, but the riverine

593   sediment flux is below 10 g m^{-1} s^{-1}. Throughout the wet summer season, substantial

594   amounts of riverine sediment are deposited near the estuary (Figure 5d), particularly

595   leading to notably high deposition of riverine sediment near the river mouth (> 100

596   mm). Outside the estuary, the thickness of riverine sediment is comparatively lower,

597   but it can reach approximately ~0.5 mm during the wet summer season in certain

598   areas off the western Guangdong coast.

599
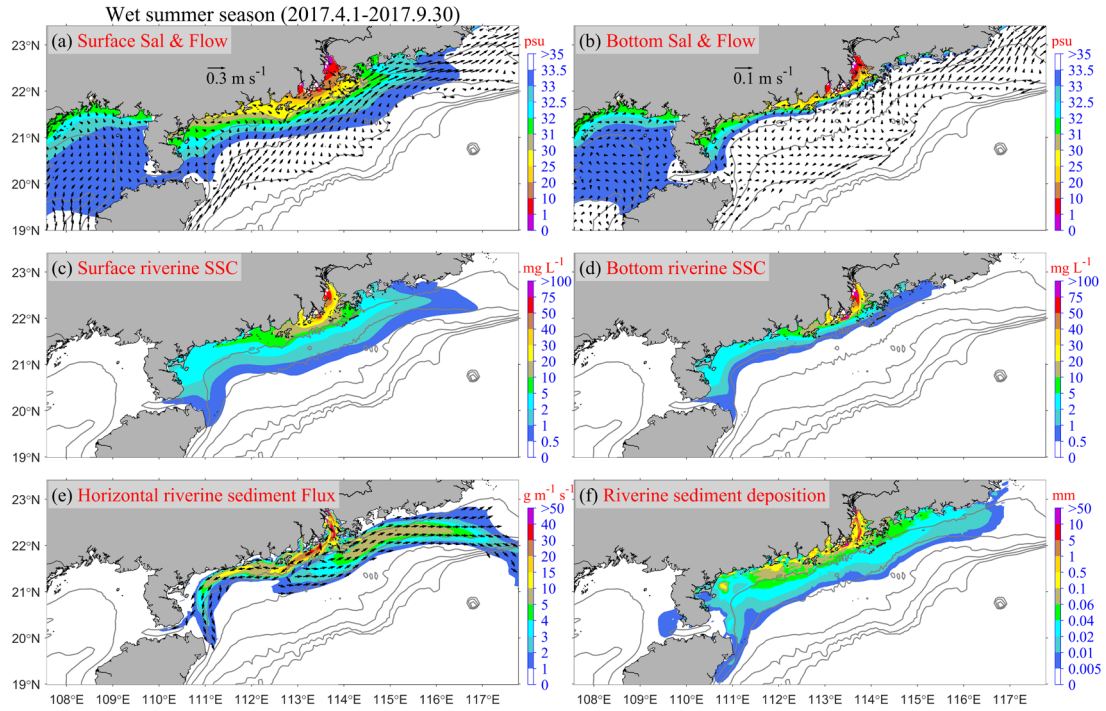
Figure 5. Patterns averaged over the entire wet summer season in the Control case: (a)

surface and (b) bottom salinity (color, psu) and flow (arrows, m s^{-1}); (c) surface and (d)

bottom riverine (classes 4 and 5 in Table 1, as follows) SSC (mg L^{-1}); (e)

depth-integrated horizontal riverine sediment transport rate (color, g m^{-1} s^{-1}) and

direction (arrows); and (f) riverine sediment deposition thickness (mm) on the seabed

during the wet summer season. Flow vectors in regions with water depths exceeding

100 m are masked for clarity.

In contrast, during winter, when river discharge is low and vertical mixing is

more intense, the correlation between the buoyant plume and riverine SSC is much

weaker, and the riverine SSC is largely governed by resuspension processes driven by

strong northeasterly winds and waves, rather than by freshwater transport. The

expansion of the Pearl River buoyant plume is constrained to the southwestward

613   direction by strong northeasterly winds (Figure 6a), resulting in a narrow cross-shore

614   width of the buoyant plume and the formation of a strong horizontal salinity gradient

615   (i.e., a salinity front, particularly within the 30–33.5 psu range shown in Figure 6a)

616   outside the estuary (Figure 6a). Flow velocity increases near this salinity front,

617   facilitating the westward extension of the buoyant plume through the Qiongzhou

618   Strait into the "Gulf" region. The riverine SSC is significantly lower than in the wet

619   summer: in the ETM zone inside the PRE, riverine SSC falls from roughly 100 mg L^{-1}

620   in summer to about 10 mg L^{-1}, while on the offshore shelf, it decreases from

621   approximately 5 mg L^{-1} to around 2 mg L^{-1} (Figures 6c-d vs. 5c-d). During the dry

622   winter, following the coastal current, the riverine suspended sediment primarily

623   moves southwestward along the coast, deflecting southward along the topography

624   near the Leizhou Peninsula (Figure 6c). It then bifurcates near the east entrance of the

625   Qiongzhou Strait, with one branch continuing into the "Gulf" region, and the other

626   one proceeding southward along the east coast of Hainan Island. Stronger winds and

627   waves in the dry winter lead to the resuspension of a considerable amount of riverine

628   sediments, originally deposited in "Proximal", "Western", and "Eastern" regions

629   during summer. The resuspended sediments are then transported to coastal bays as

630   well as to the sides and rears of the islands (Figure 6d). Additionally, a portion of the

631   riverine sediment transported to the "Gulf" region gets deposited on the seabed during

632   the dry winter season.

633
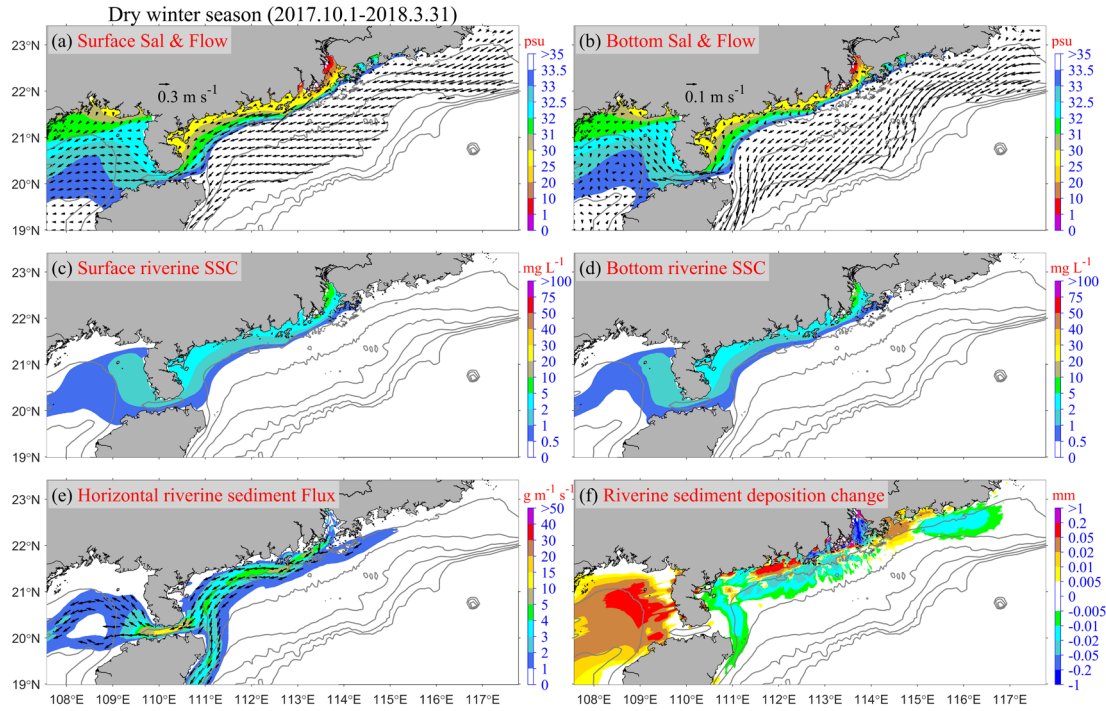
Figure 6. Same as Figure 5, but for the dry winter season in the Control case. Notably,

(f) illustrates the changes in riverine sediment (classes 4 and 5 in Table 1) deposition

on the seabed at the end of the dry winter season compared to the end of the wet

summer season.

3.2 Riverine sediment budgets and annual deposition over the shelf

We present the sediment fluxes and retention amounts in different regions. Figure

7a-c illustrates the proportion of riverine sediment retention budget within each region,

expressed as a percentage of the total annual river sediment load input (Figures 3a),

for the wet summer season (Figure 7a), the dry winter season (Figure 7b), and the

entire year (Figure 7c), based on ~~under~~ the Control run ~~case~~, respectively. Meanwhile,

Figure 7d illustrates the annual deposition over the shelf.

The retention of Pearl River sediment on the continental shelf exhibits significant

seasonal variations (Figures 7a-c). During the wet summer (characterized by high

discharge and relatively calm ~~low~~ wind/waves), the PRE and continental shelf receive

95.17% of the annual sediment input ~~load from the Pearl River~~ (Figures 3a and 7a).

Of this, about ~~Approximately~~ two-thirds ~~of this sediment~~ is retained in the "Proximal"

region (Figure 7a). Influenced~~Additionally, influenced~~ by the prevailing southerly

winds and northeastward shelf currents~~circulation~~, 13.01% of the annual sediment

load is retained in the "Eastern" and "Southeastern" regions (Figure 7a). Meanwhile,

the shelf west of the PRE (⑤−⑧ regions) retains 15.87% of the annual load, with the

"Western" region alone ~~being the primary receiver,~~ accounting for 8.48% (Figure 7a).

In contrast, only ~~Only~~ 0.92% and 2.3% ~~of the annual load~~ enter the more remote

"Gulf" and "Distal" regions, respectively~~, during summer~~ (Figure 7a). The "Southern"

region retains a mere 1.22% of the sediment (Figure 7a).

In the dry winter (characterized by low discharge and energetic winds/waves), the

PRE and the continental shelf receive only 4.83% of the annual sediment load

(Figures 3a and 7b). The sediment distribution during this season ~~is~~ primarily reflects~~a~~

~~result of the dynamic~~ reworking of previously retained ~~the~~ sediments ~~of~~ from summer

~~deposition~~ (Figure 7b). Retention in ~~While~~ the "Proximal" region ~~continues to receive~~

~~sediment, with a 1.38%~~ increases slightly (+1.38%)in retention, while retention

decreases in the ②−⑥ regions ~~experience a decrease in sediment retention~~. Much of

this remobilized sediment~~This sediment~~ is ~~predominantly~~ transported farther offshore

and retained in the ~~more distant~~ "Gulf" and "Distal" regions (Figure 7b).

The annual sediment budget reveals that 66.45% of the Pearl River sediment is

670 retained in the "Proximal" region (Figure 7c). Additionally, 9.2% is retained in the

671 "Eastern" and "Southeastern" regions (Figure 7c), primarily during summer (Figures

672 7a vs. 7c), while 24.12% is retained on the shelf west of the PRE (⑤–⑧ regions),

673 with most of that occurring the majority in the "Gulf" and "Distal" regions, mainly

674 during winter (Figures 7b vs. 7c).

675   The annual deposition thickness of the Pearl River-derived sediments (Figure 7d),

676 as illustrated in Figure 7d, reveals significant deposition within the "Proximal" region,

677 with many areas exceeding 10 mm despite wintertime resuspension and

678 redistributiontransport. Additionally, deposition on In the "Eastern" region, deposition

679 reached reaches a magnitude of 0.1 mm, while the western inner shelf west of the

680 PRE ("Western" and "Gulf" regions) exhibited exhibits significantly greater

681 accumulation. For instance, the deposition west of the Chuanshan Islands reached a

682 magnitude of 0.5 mm. In the "Gulf" region, deposition was is primarily concentrated

683 in the northeastern part, extending southwestward along the 30-60 m isobaths.

684 Sediments transported southwestward along the east coast of Hainan Island and

685 intoretained in the "Distal" regions did not predominantly settle on the seabed due to

686 the greater water depth but remained largely suspended in the water column due to the

687 greater water depth, with limited deposition on the seabed.

688

Figure 7. Riverine sediment (classes 4 and 5 in Table 1) retention budget percentages at eight regions (see Figure 1) during (a) the wet summer season, (b) the dry winter season, and (c) the entire year in the Control run case. (d) the annual deposition patterns spanning from April 1st, 2017, to March 31st, 2018 in the Control Run. All percentages displayed in the figure are relative to the annual riverine sediment load

696   (see Figure 3a). The black percentage values represent the combined total of riverine

697   sediment Class 4 and Class 5, while the red and blue values denote sediment Class 4

698   and Class 5, respectively. Arrows indicate the direction of net riverine sediment flux

699   at each transect during the specified period.

700

701 **3.3 Model sensitivity experiments: relative roles of physical**

702 **drivers~~processes~~, sediment properties, and spin-up durations**

703   Six sensitivity simulations, namely Exp 2-7 (NTS, NWS, NAS, NVS, DSV, and

704   Cycle), were conducted (Table 2). As the latter three experiments do not impact

705   hydrodynamics, we focus on presenting the seasonal mean differences in bottom shear

706   stress between the Control run and the first three cases (NTS-Control, NWS-Control,

707   NAS-Control) for both summer and winter (Figure 8).

708   In the NTS case, bottom shear stress is reduced relative to the Control run by a

709   similar amount in both summer and winter due to the minimal seasonal variation in

710   tidal intensity. This reduction primarily occurs in the PRE, around the Taiwan Bank,

711   and near the Leizhou Peninsula (Figures 8a-b). In contrast, in the NWS case, the

712   reduction in bottom shear stress is greater in winter than in summer, reflecting the

713   intense seasonal variability of wind and wave activities (Figures 3b, 3d-e, and 4a-f).

714   Unlike the NTS case, the NWS-induced decrease occurs mainly in the nearshore areas

715   outside the PRE, although similar declines are also found around the Taiwan Bank and

716   along the eastern side of the Leizhou Peninsula (Figures 8c-d). For the NAS case, the

717   impact on bottom stress is minimal compared to the NTS and NWS cases. The effect

718 is almost negligible on the inner shelf at depths less than 100 m, with widespread

719 impacts generally below 0.02 Pa. Some pronounced deviations are noted in localized

720 deeper areas near the southern boundary of the domain (Figures 8e-f). These

721 deviations, likely arising from boundary condition effects, are situated far from the

722 Pearl River-derived sediment distribution areas (Figures 5-6). Consequently, they do

723 not influence the dynamics of the Pearl River-derived sediment transport over the

724 continental shelf (Figures 8e-f).

725
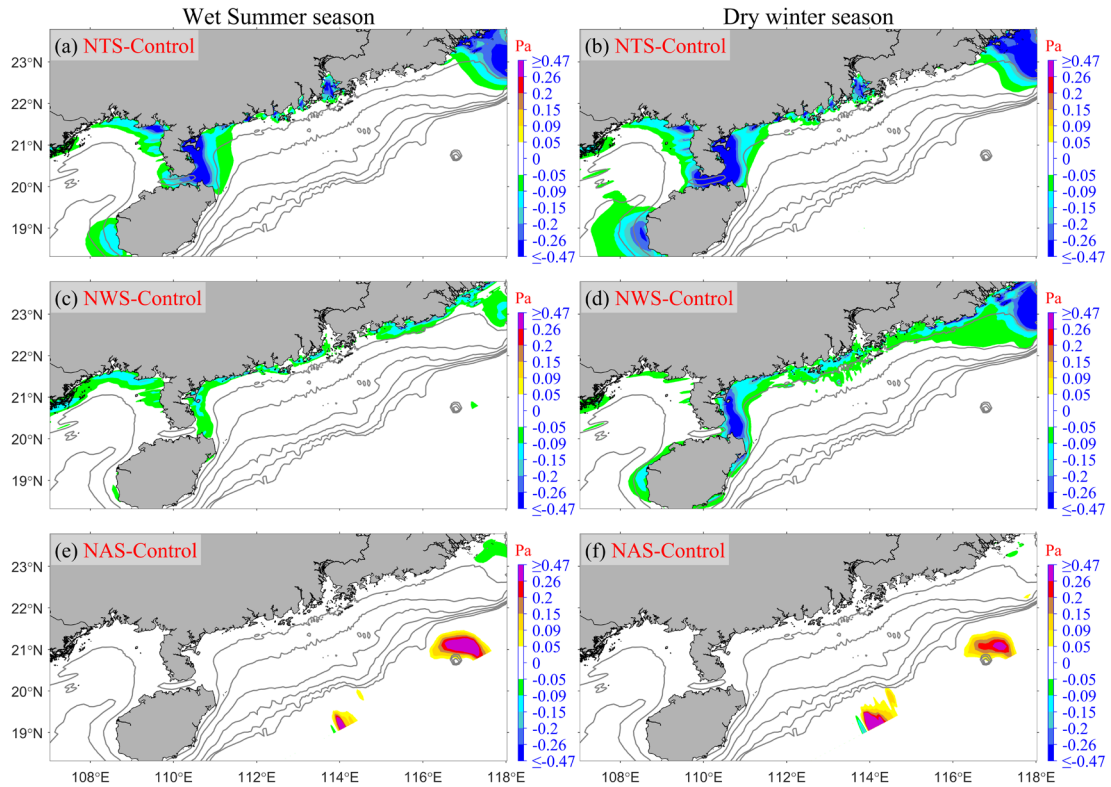
727 **Figure 8.** The seasonal mean differences in bottom shear stress between the Control

728 run and the following cases: (a-b) NTS (NTS minus Control), (c-d) NWS (NWS

729 minus Control), and (e-f) NAS (NAS minus Control). The first column represents the

730 wet summer season, while the second column corresponds to the dry winter season.

731

Then, we analyzed seasonal riverine sediment transport and deposition patterns

("riverine" means only the Pearl River-derived sediment, classes 4-5 in Table 1, as

follows) by comparing the control run with six sensitivity experiments (NTS-Control,

NWS-Control, NAS-Control, NVS-Control, DSV-Control, and Cycle-Control)

(Figures 9-11). The study focuses on the Pearl River-derived sediment dynamics,

indicated by surface circulation and riverine SSC distribution patterns (Figures 5 and

6). Specifically, Figures 9 and 10 present seasonal surface currents and SSC

differences between control and sensitivity runs, complemented by deposition pattern

differences in Figure 11.

Compared to the Control case, the NTS case demonstrates that ~~while~~ tides

significantly enhance bottom stress (Figures 8a-b), while ~~but~~ have minimal impact on

the mean circulation (Figures 5a, 6a, and 9a-b), and their exclusion reduces bottom

shear stress by over 0.2 Pa in the PRE and near the Leizhou Peninsula. Consequently,

increased deposition of the Pearl River-derived sediments occurs inside the PRE, its

adjacent areas, and on both sides of the Leizhou Peninsula (Figure 11a). During

summer, riverine SSC notably decreases in the ①−⑥ regions (Figure 9a). This

reduction pattern persists in winter, particularly in the PRE and on both sides of the

Leizhou Peninsula (Figure 9b).

Like the NTS, NWS has a relatively minor impact on circulation (Figures 5a, 6a,

and 9c-d). However, NWS leads to more Pearl River-derived sediment being

deposited in the nearshores of "Western" and "Eastern" regions (Figure 11b).

753   Consequently, the riverine SSC in summer is much lower in the downstream of the

754   PRE and in ②−⑥ regions (Figure 9c). This similar reduction pattern persists in the

755   winter, but is slightly in more western regions (Figure 9d).

756   For the NAS case, the impact on bottom stress is minimal compared to the NTS

757   and NWS cases. However, NAS has a relatively large impact on the mean circulation

758   (Figures 5a, 6a, and 9e-f). It mainly influences the summer circulation. Specifically,

759   ignoring these factors would cause the relatively strong northeastward flow along the

760   Guangdong coast to become very weak (Figure 9e). When it comes to winter, the

761   influence of NAS on circulation is relatively small. That is, in the absence of the

762   background residual water level and residual circulation, due to the strong

763   northeasterly winds in winter, the overall circulation is still southwestward (Figure 9f).

764   The decreased northeastward flow in summer leads to the Riverine SSC being

765   scarcely transported to the vicinity of the "Eastern" and "Southeastern" regions.

766   Consequently, the Riverine SSC there is decreased (Figure 9e) and sediment

767   deposition is significantly reduced (Figure 11c). Most of the suspended Riverine

768   sediment is transported southwestward, resulting in an increase in the Riverine SSC

769   along the "Western" region. In winter, since most of the suspended Riverine sediment

770   has been transported southwestward in summer, the Riverine SSC decreases

771   compared to the Control run (Figure 9f). Ultimately, NAS mainly causes a significant

772   reduction in sediment deposition in the "Eastern" region, while sediment deposition

773   increases in the "Gulf" and the "Distal" regions (Figure 11c).

774
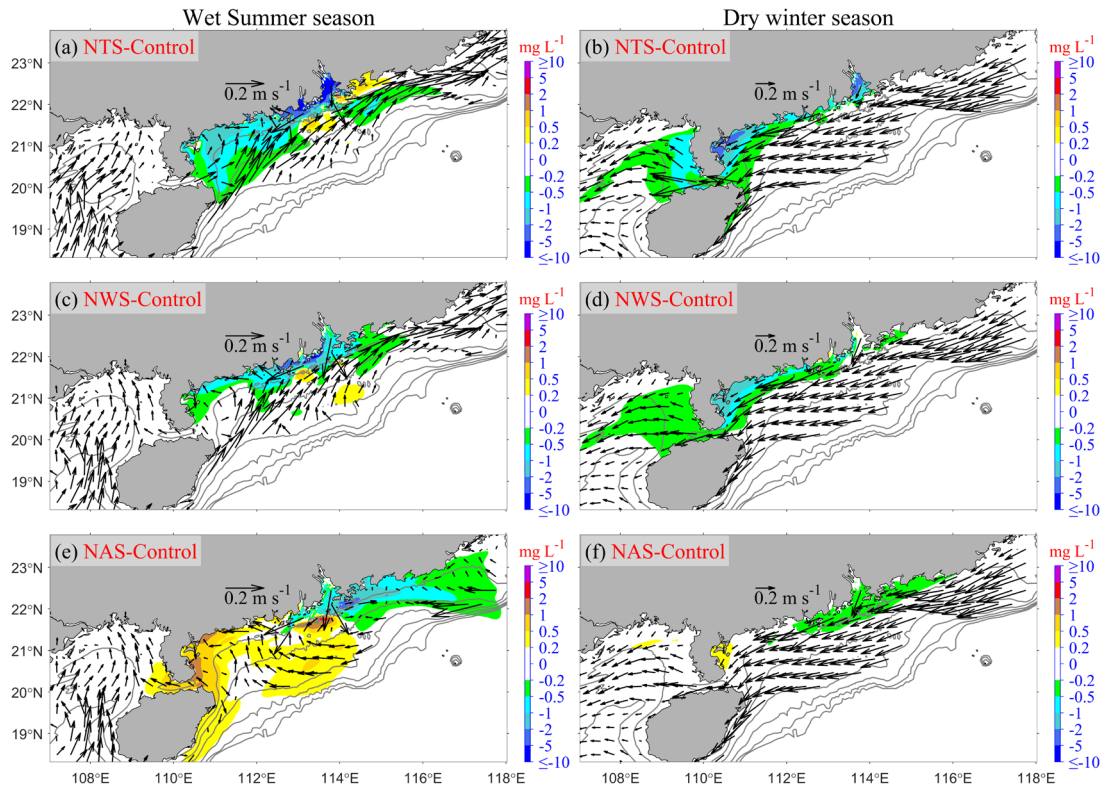
Figure 9. Same as Figure 8, but for seasonal mean differences in surface riverine SSC between the Control run and the following cases: (a-b) NTS-Control, (c-d) NWS-Control, and (e-f) NAS-Control. The first column represents the wet summer season, while the second column corresponds to the dry winter season. Vectors show the seasonal mean surface current fields in each experiment. Note that the riverine SSC values shown in the figure correspond to classes 4 and 5 as defined in Table 1.

For the NVS case, the summer conditions of NVS are precisely the same as those of the Control run (Figure 10a). Since the critical shear stress for erosion in winter is lower than that in the Control run, this leads to an increase in re-suspension in the "Proximal", "Western" and the "Gulf" regions, increasing Riverine SSC (Figure 10b).

788   Eventually, this causes a reduction in the deposition thickness of the Pearl

789   River-derived sediments in these regions (Figure 11d).

790   In the DSV case, significant reductions occur in the primarily high SSC areas in

791   the Control run in both summer and winter (Figures 5c, 6c, 10c-d). The enhanced

792   settling velocity results in an increased deposition of Pearl River-derived sediments

793   along the Guangdong coastline ("Western" and "Eastern" regions) and the eastern

794   "Gulf" region, accompanied by a reduced deposition thickness in the western "Gulf"

795   region (Figure 11e).

796   In the Cycle case, the new riverine sediment input and its transport processes

797   during the Cycle experiment are nearly identical to those in the Control run. Therefore,

798   compared to the Control run, the Cycle experiment specifically focuses on examining

799   the impact of the presence of pre-existing Pearl River-derived sediments on estimating

800   the riverine SSC and the annual seabed riverine sediment budget in the second year.

801   Consequently, during the summer period, the Cycle case experiences elevated riverine

802   SSC in the primary depocenters identified in the Control run (Figures 7d and 10e),

803   while this effect is diminished by winter (Figure 10f). Figure 11f thus captures the

804   transport trends of pre-existing riverine sediments in the second year, demonstrating

805   that riverine sediments deposited during the first year can be resuspended and

806   transported further southwestward during the second year. This migration is driven by

807   the annually averaged net alongshore coastal current, which remains predominantly

808   directed toward the southwest. The current becomes stronger during the winter

809   monsoon under the influence of prevailing northeasterly winds, whereas the opposing

810   summer southerly winds are comparatively weaker, indicating a persistent

811   southwestward sediment transport trend over multi-year timescales.

812

813
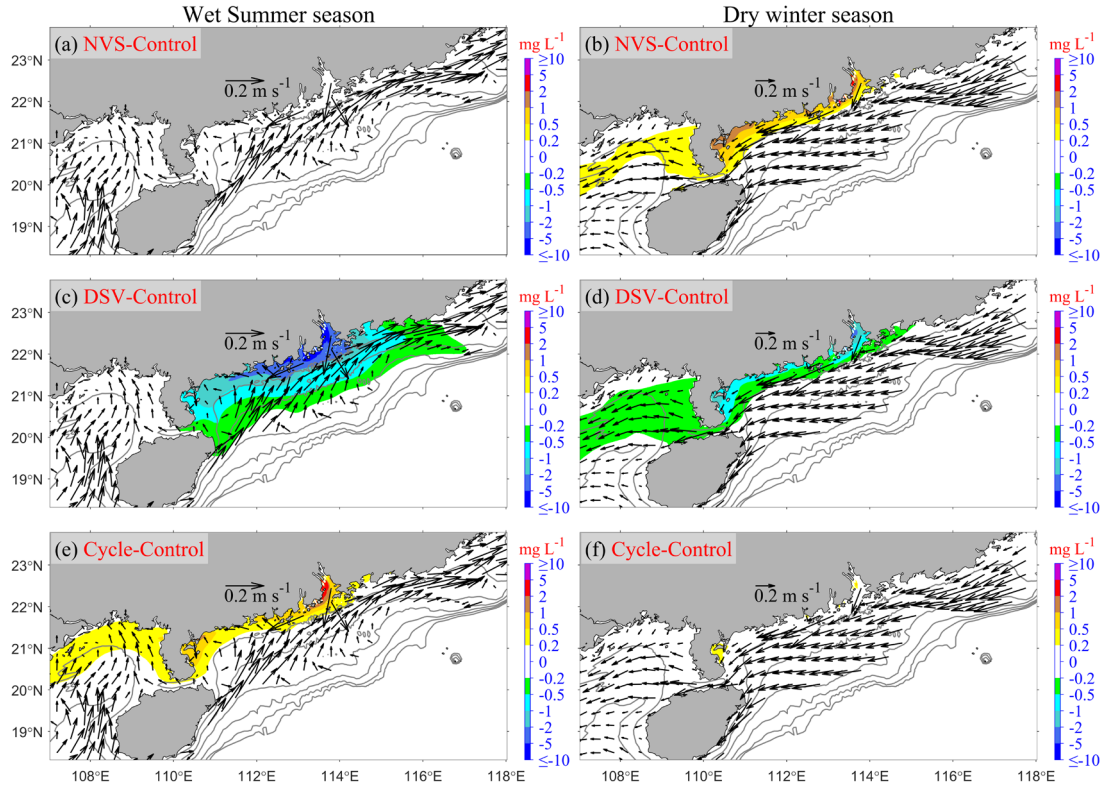
814   **Figure 10.** Same as Figure 9, but for the latter three experiments (NVS, DSV, Cycle).

815   (a-b) NVS-Control, (c-d) DSV-Control, and (e-f) Cycle-Control.

816
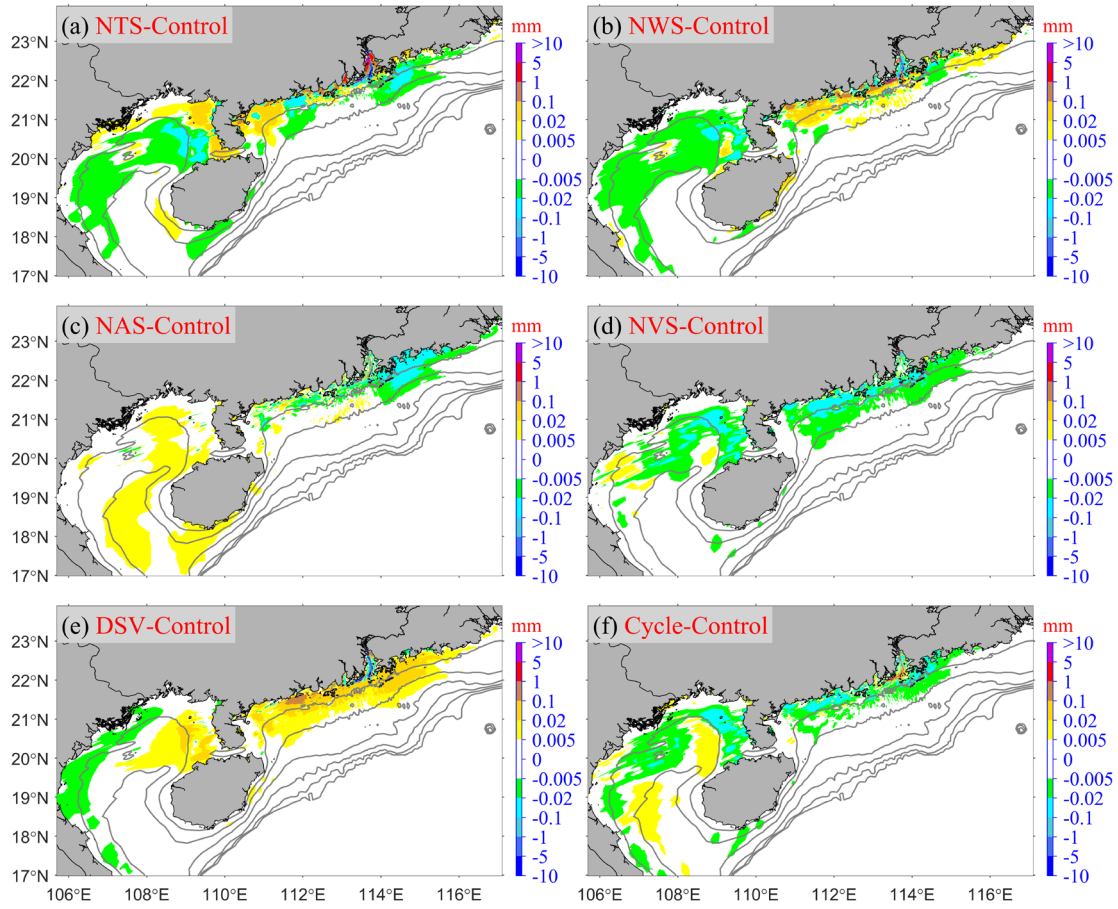
Figure 11. The differences in annual deposition patterns of Pearl River-derived sediment (classes 4-5, Table 1) on the seabed between the Control run and the following cases: (a) NTS-Control, (b) NWS-Control, (c) NAS-Control, (d) NVS-Control, (e) DSV-Control, and (f) Cycle-Control.

3.4 Modeled regional retention budgets in sensitivity experiments

Finally, we analyze the impact of various factors on the annual riverine sediment retention budget across different regions. Specifically, Figure 12 illustrates the annual riverine sediment retention budget in various regions under six sensitivity simulations, namely Exp 2-7 (including NTS, NWS, NAS, NVS, DSV, and Cycle). It should be

828   noted that the retention percentages budget and their variations discussed hereinafter

829   are all relative to the annual riverine sediment load (Figure 3a).

830   As shown in Figure 12, tides and sediment settling velocity have the most

831   significant impact on the retention in the "Proximal" region. In the NTS case and the

832   DSV case, the retention in the "Proximal" region is 70.92% and 71.57%, respectively

833   (Figures 12a and 12e), which is higher than 66.45% in the Control run (Figure 7c).

834   This indicates that ignoring tides will cause the "Proximal" region to capture more

835   riverine sediments, and a larger settling velocity will result in more riverine sediments

836   being retained within the "Proximal" region. In these two cases, compared with the

837   Control run, the retention in the "Gulf" and "Distal" regions decreases. Meanwhile,

838   the DSV case causes the greatest increase in retention in the "Western" region, with an

839   increase of +1.91%.

840   Furthermore, the NWS also leads to a 2.2% increase in retention in the

841   "Proximal" region (Figure 12b), which is lower than that in the NTS case. This shows

842   that tides dominate resuspension versus deposition in the "Proximal" region more than

843   waves do. However, for the "Western" region, compared with the NTS case, the NWS

844   causes a greater increase in retention, indicating that waves dominate the resuspension

845   of Pearl River-derived sediments in these nearshore areas more than tides do.

846   For the "Eastern" and "Southeastern" regions, NAS brings about the most

847   dramatic changes, the retention of Pearl River-derived sediments in these regions

848   drops from 9.1% to 0.84% compared to the Control run (Figure 12c). Meanwhile,

849   ignoring these background circulations results in a substantial increase in the retention

850   in the "Distal" region, with an increase of 6.49%.

851   The NVS case leads to a decrease in the retention of the Pearl River-derived

852   sediments in ①−⑥ regions compared to the Control run. The reduction ranges from

853   -0.05% to -0.85% (Figure 12d), which in turn causes the retention in the "Gulf" and

854   "Distal" regions to increase by 0.7% and 1.47%, respectively. Overall, compared with

855   scenarios that ignore physical drivers processes and alter sediment settling velocity

856   (NTS, NWS, NAS, and DSV), the NVS scenario has a relatively smaller impact on

857   the retention of the Pearl River-derived sediments.

858   Finally, in the Cycle case, to isolate the pre-existing Pearl River-derived

859   sediments, the initial retentions (the end conditions of the Control run on March 31,

860   2018) were subtracted before calculating the retention in the Cycle case (Figure 12f).

861   The retention of Pearl River-derived sediments in ①−⑥ regions shows little

862   variation, with values ranging from -0.98% to +0.24% compared to the Control run

863   (Figure 12f). The most significant changes are the decreases and increases in retention

864   in the "Gulf" and "Distal" regions, which are -2.17% and +3.54%, respectively. This

865   demonstrates the long-term trend of southwestward transport of Pearl River-derived

866   sediments on the shelf (relative to the Control run).

867

868
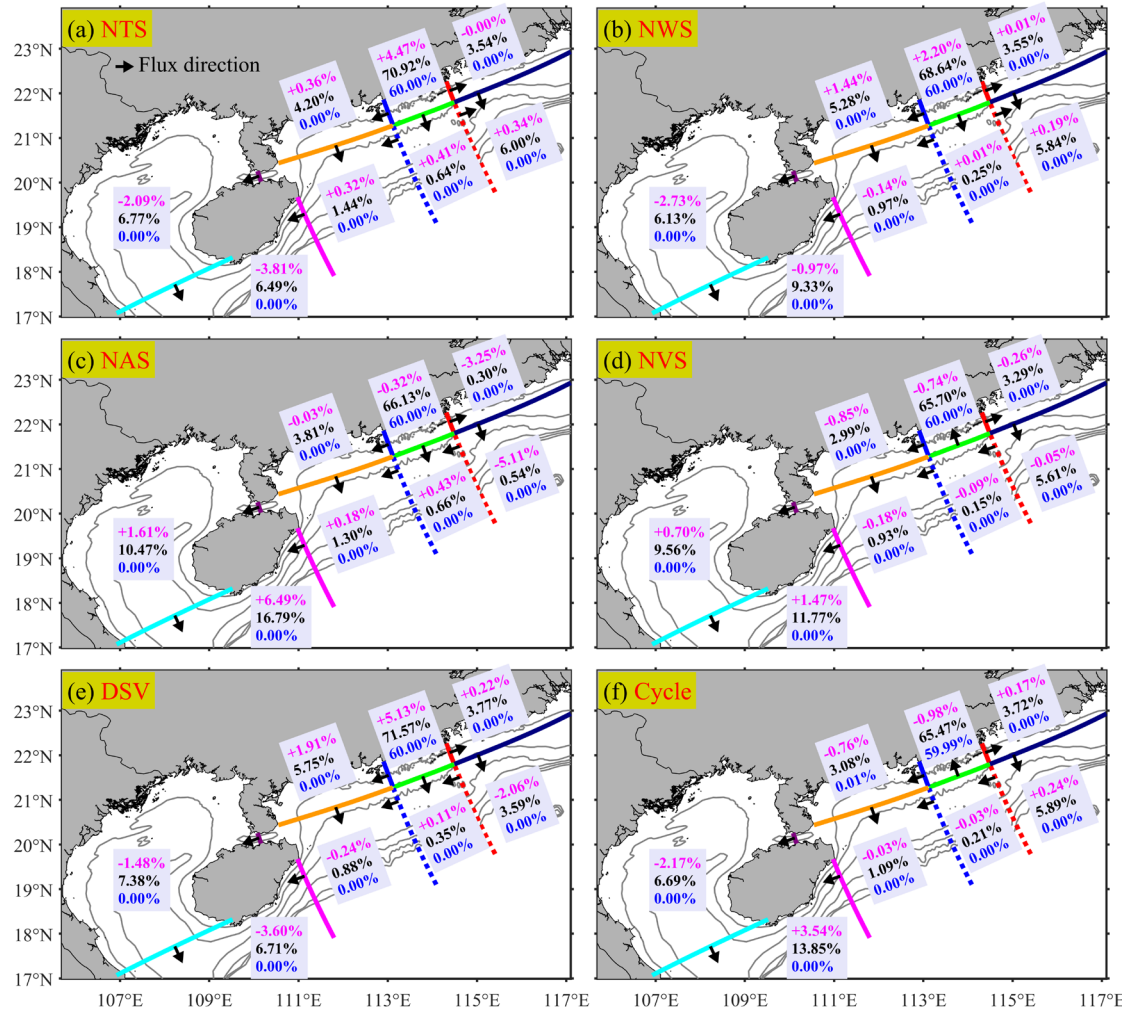
Figure 12. Same as Figure 7c, but for the other six cases: (a) NTS, (b) NWS, (c) NAS,

(d) NVS, (e) DSV, and (f) Cycle, respectively. All percentages shown in the figure are

expressed relative to the annual riverine sediment load (see Figure 3a). Magenta

values denote the differences in retention percentage of riverine sediments (Classes 4

and 5; Table 1) between the Control run and each sensitivity case. Black values

represent the combined retention of Classes 4 + 5, while blue values indicate Class 5

alone. To obtain the retention percentage for Class 4, simply subtract the Class 5

percentage (blue) from the combined Classes 4 + 5 percentage (black).

877

878

4. Discussions

4.1 Fidelity of our model results

We simulated the suspension, transport, and deposition of the Pearl River-derived sediment over the shelf from April 2017 to March 2018. Comparisons with multiple types of observations demonstrated that the model simulation reasonably well captured the regional patterns and temporal variability of water levels (Figures S2-S4), surface waves (Figures S5-S6), estuarine and shelf currents (Figures S8a-b and S9-S10), salinity and temperature (Figures S7a-b and S8c-d), and SSC (Figures S7c and S8e-f). Even though we have made substantial efforts to collect observational data and conduct calibration and validation, the large scope of the study area and the fact that the study covers an entire year mean that there are some inherent challenges to achieving a complete analysis. The real-world situation may be extremely complex, and these validations may still not be sufficient to address all issues (such as the accurate parameterization of sediment characteristics and their seasonal variations, as well as the proportion of slow-settling fine grains and flocculated flocs in riverine sediments). Therefore, in this section, we intend to discuss the fidelity of our results.

Studies have demonstrated a seasonal dependence of sediment critical shear stress (Xu et al., 2014; Briggs et al., 2015). On the Louisiana shelf, seabed erodibility is controlled by grain size, sediment age, proximity to river sources, bioturbation, and flood deposits, and is higher during the wet season than the dry season (Xu et al., 2014). It is also linked to seasonal hypoxia: sites experiencing hypoxic (hypoxia greater than 75% of the time, hypoxia defined as < 2 mg O_2 L^{-1}) conditions exhibit

901 greater erodibility, whereas the normoxic (hypoxia less than 25% of the time) site

902 shows the lowest erodibility (Briggs et al., 2015). These findings imply that sediment

903 models should incorporate seasonal variations in critical shear stress, parameterized

904 using field observations or seasonal sampling data. Similarly, in the PRE, field

905 observations, laboratory experiments, and numerical sensitivity analyses have shown

906 that the critical shear stress for erosion of sediments in the PRE is higher in winter/dry

907 season than in summer/wet season (Dong et al., 2020; Cao et al., 2025). The summer

908 period in the PRE also coincides with seasonal hypoxia (Cui et al., 2018; Cui et al.,

909 2022), which likely contributes to this seasonal variation in erodibility. Therefore, we

910 considered the seasonal variation of critical shear stress for erosion in a suite of model

911 experiments, that is, increasing the critical shear stress for erosion in winter. This

912 setting was also applied during the 15-month spin-up before conducting the model

913 experiments (the spin-up employed the same forcing conditions and model settings as

914 the Control run to maintain consistency~~the driving force of the spin-up is realistic, i.e.,~~

915 ~~the settings are consistent with those of the Control run~~). After ~~realistic reworking~~

916 ~~during~~ the spin-up, the bed sediment grain size distribution (used as initial conditions

917 in the Control run and all Sensitivity cases except the Cycle case) is quite close to the

918 initial prototype (Figures 2d-f vs. 2g-i).

919 When the seasonal variation of critical shear stress for erosion is omitted (NVS

920 case), the model results suggest a reduced retention of Pearl River-derived sediments

921 in ①−⑥ regions during winter, alongside an increased retention in the "Gulf" and

922 "Distal" regions. However, these differences are relatively small in magnitude

923   compared to the annual load (Figure 12d). Thus, accounting for seasonal variations in

924   critical shear stress for erosion has a limited influence on the annual-scale retention

925   patterns. The dispersal distance of fluvial sediments on continental shelves is strongly

926   influenced by settling velocity (Harris et al., 2008). For example, Apennine-derived

927   sediments, characterized by lower settling velocities, travel farther before deposition

928   than Po River sediments, which are predominantly flocculated and settle more rapidly

929   (Fox et al., 2004; Harris et al., 2008). Likewise, our results suggest that selecting an

930   appropriate settling velocity parameter exerts a greater control on sediment dispersal

931   patterns than accounting for seasonal variations in critical shear stress for erosion

932   (Figure 12d vs. 12e). The results of the DSV case show that a sediment settling

933   velocity twice that of the Control run leads to the highest retention in the "Proximal"

934   and "Western" regions across all experiments (Figure 12e), while reducing the

935   retention in the "Distal" region (Figure 12e). Although the settling velocity we

936   adopted is based on previous studies (Xia et al., 2004) and model calibrations (Figures

937   S7c and S8e-f), with due consideration given to the presence of slow-settling single

938   fine grains and high-settling flocs in riverine sediments, certain discrepancies might

939   still exist in this setting. These discrepancies are contingent upon the actual magnitude

940   of the low settling velocity of fine grains. In almost all cases, all flocs in the model are

941   retained in the "Proximal" region (Figure 12a-e), and only in the Cycle case, flocs

942   accounting for 0.01% of the annual load are retained in the "Western" region west of

943   the "Proximal" region (Figure 12f, blue values), indicating that high-settling flocs

944   hardly leave the "Proximal" region. This finding shows close alignment with, yet

945 exhibits minor distinctions from, the observed patterns in the Mekong Shelf (Xue et

946 al., 2012). Xue et al. (2012) found that while the preponderance of flocs is deposited

947 on the Mekong delta front precisely at the river mouth, a quantity equivalent to 1.6%

948 of the annual riverine sediment load of flocs is deposited on the downdrift delta front

949 further downstream from the river mouth. This is mainly because the estuarine bay of

950 the PRE is wider and there are numerous islands near the river mouth. The

951 overwhelming majority of flocs are either deposited within the estuarine bay or

952 captured by the surrounding islands. In conclusion, our results are affected by the

953 settling velocity of fine grains. More field observations and studies on model

954 parameterization regarding the settling velocity of fine grains are urgently needed.

955 As previously noted, we classified riverine sediments into two categories based

956 on established research: 40% slow-settling fine grains and 60% fast-settling flocs.

957 This 40%/60% distribution is consistent with the setting from earlier studies (Zhang et

958 al., 2019; Zhang et al., 2021), as summarized in Table 1. While such assumptions are

959 necessary for modeling purposes, the actual composition of riverine sediments in

960 natural environments remains uncertain. To evaluate the sensitivity of our results to

961 this uncertainty, we conducted a conceptual analysis. If all riverine sediments were

962 hypothetically composed entirely of fast-settling flocs, they would be completely

963 retained near the source, with no transport to the "Gulf" region. However, this

964 scenario is inconsistent with the radionuclide measurements obtained from "Gulf"

965 region surface sediment samples (Lin et al., 2020). On the other hand, if all sediments

966 were considered slow-settling fine grains, only 16.13% would be retained in

"Proximal" region under normal conditions (or 28.9% in the DSV case), a result that

diverges significantly from established research.

Chen et al. (2023) analyzed high-resolution seismic data and demonstrated that

approximately 35% of the Pearl River-derived sediment has been transported to

offshore shelf areas over the past 6,500 years, suggesting that 65% was deposited

proximally. Our findings are in close agreement, indicating that 66.45% of the Pearl

River sediments are retained in the proximal region, while 33.55% are transported

elsewhere. This consistency with Chen et al. (2023) supports the validity of our

approach. Taken together, these analyses confirm that the 40%/60% fraction

assumption is a reasonable approximation for modeling purposes.

Furthermore, our model results demonstrate reasonable reliability in other aspects.

Liu et al. (2009) and Ge et al. (2014) using chirp sonar profiles from the inner shelf of

the South China Sea combined with Zong et al. (2009)'s onshore borehole data, found

that the thickness of Pearl River-derived sediments within the PRE since the Holocene

is over 20 m, while the mud thickness in the shallow waters west of the Chuanshan

Islands (see Figure 1) is approximately 5-10 m. Our calculated annual sediment

thicknesses for these two regions are approximately 2 mm and 0.3 mm (Figure 7d),

respectively. Given our model's annual riverine sediment load of 34.52 megatons,

which has been significantly reduced due to recent human activities (Dai et al., 2008),

compared to the widely accepted Holocene average of around 90 megatons (Liu et al.,

2009), we estimate the total sediment thickness over the past 7500 years to be roughly

39 meters and 6 meters for these depositional zones, consistent with previous studies

989   (Liu et al., 2009; Zong et al., 2009).

990   Furthermore, our results reveal that 8.86% of the riverine sediment derived from

991   the Pearl River is transported to the "Gulf" region (Figure 7c), primarily during the

992   winter season (Figure 7b). This finding is not only consistent with the earlier

993   speculation proposed by Ge et al. (2014) but also supplements the conclusions drawn

994   by Lin et al. (2020). From a hydrodynamic perspective, Shi et al. (2002) found that

995   the net flux of currents in the Qiongzhou Strait is westward throughout the year. Our

996   results for both wet summer (Figures 5a-b) and dry winter currents (Figures 6a-b) in

997   the Qiongzhou Strait are consistent with Shi et al. (2002). This westward flow

998   contributes to the westward transport of Pearl River sediment to the "Gulf" region.

4.2 Implications of our model results

1000   The fate of sediment dispersed from the river into the coastal ocean involves at

1001   least four processes: supply via buoyant plumes; initial deposition; resuspension and

1002   transport by marine processes; and long-term net accumulation (Wright and Nittrouer,

1003   1995). In general, a significant proportion of river sediment tends to deposit in the

1004   estuary and its vicinity (Walsh and Nittrouer, 2009; Hanebuth et al., 2015).

1005   Walsh and Nittrouer (2009) present a hierarchical decision tree designed to

1006   predict the marine dispersal system at a river mouth based on fundamental

1007   oceanographic and morphological characteristics. Within this framework, riverine

1008   sediment deposition is characterized using key factors, including riverine sediment

1009   discharge (greater or less than 2 megatons), shelf width (greater or less than 12 km),

1010   and wave and tidal range conditions (greater or less than 2 m) (Walsh and Nittrouer,

1011 2009).

1012 We aim to analyze our PRE simulation results using the framework established

1013 by Walsh and Nittrouer (2009). Although the Pearl River's annual riverine sediment

1014 discharge (Figure 2a) exceeds the Walsh and Nittrouer (2009)'s 2 megatons per year

1015 threshold, most of the sediment still remains deposited near the estuary (Figure 7c),

1016 indicating an estuarine accumulation-dominated (EAD) system. This behavior

1017 deviates from the predictions of, unlike the hierarchical decision tree proposed by

1018 Walsh and Nittrouer (2009). Outside the estuary, the continental shelf, spanning

1019 200-220 km in width (Liu et al., 2014), significantly exceeds Walsh and Nittrouer

1020 (2009)'s 12 km threshold. As a result, most escaped riverine sediments tend to

1021 accumulate on the shelf rather than being captured by submarine canyons (Figures

1022 7c-d). This wide, shallow shelf promotes sediment deposition and limits the direct

1023 transport of fine sediments into deeper waters (Walsh and Nittrouer, 2009).

1024 Subsequently, given that the annual mean tidal range (Chen et al., 2016; Gong et al.,

1025 2018b) and Hsig (Figure 3d) near the PRE are both below the 2 m threshold

1026 established by Walsh and Nittrouer (2009), the majority of escaped riverine sediments

1027 are predominantly deposited in the proximal depo-center. Our findings demonstrate

1028 that most of our outcomes are consistent with the hierarchical decision tree proposed

1029 by Walsh and Nittrouer (2009), except for the application of the 2 megatons per year

1030 threshold for riverine sediment discharge. This phenomenon can primarily be

1031 attributed to the unique geomorphological characteristics of the PRE, including its

1032 broad mouth (Figures 1 and S1), extensive accommodation space encompassing

1033 approximately 2385 km^2 of water area (Wu et al., 2018), the presence and sheltering

1034 effect of numerous adjacent islands (Li et al., 2024b), and the division of fluvial

1035 sediment discharge through eight distinct outlets (Hu et al., 2011).

1036   The monsoonal nature of the northern SCS (Figures 4a-b) induces pronounced

1037 seasonal variations in Pearl River-derived sediment transport and deposition (Figures

1038 5 and 6). During the summer wet season, the Pearl River delivers approximately 95.17%

1039 of its annual sediment load to the PRE and the adjacent shelf (Figure 7a) under

1040 relatively calm wind and wave conditions (first column of Figure 4), leading to

1041 predominant proximal deposition (Figure 5f). In contrast, the winter dry season is

1042 characterized by strong northeasterly monsoon winds that generate high-energy waves

1043 (second column of Figure 4), significantly increasing bottom shear stress (Figures

1044 4g-h). This process resuspends previously deposited sediments and facilitates their

1045 redistribution, particularly toward regions such as the "Gulf" region (Figure 6f).

1046   The PRE exhibits distinctive geomorphological features, yet dispersal of its

1047 fine-grained sediment transport on the continental shelf conforms to general patterns

1048 observed offshore of other monsoon-influenced estuarine systems. Similar

1049 multiple-stage sediment delivery and dispersal mechanisms have been documented

1050 offshore of various major estuaries and their adjacent shelves, including the Yellow

1051 River Shelf (Bian et al., 2013; Zeng et al., 2015), Changjiang River Shelf (Zeng et al.,

1052 2015), and Mekong River Shelf (Xue et al., 2012; Eidam et al., 2017), demonstrating

1053 comparable sedimentary processes under monsoon climatic influences. In these

1054 systems, sediment transport is not confined to a single process but rather occurs in

1055 stages, influenced by seasonal variations in hydrodynamic conditions. Like the PRE

1056 Shelf, the Mekong Shelf experiences distinct phases of sediment deposition, with fine

1057 sediments being delivered during periods of high river discharge and then

1058 redistributed by waves and tidal forces, particularly during monsoonal shifts (Xue et

1059 al., 2012; Eidam et al., 2017). These complex patterns highlight the interplay between

1060 riverine inputs, coastal morphology, and oceanographic processes in shaping sediment

1061 dynamics.

1062   These sediment delivery patterns have implications beyond sediment fate,

1063 particularly for carbon cycling. Sediment deposition in coastal and shelf areas plays a

1064 significant role in trapping organic carbon, influencing long-term carbon burial rates

1065 (LaRowe et al., 2020). Sediment dynamics directly influence the fate of organic

1066 carbon (OC) in marine environments, where sediments function as both a sink and a

1067 source of OC, playing a pivotal role in global carbon cycling (Repasch et al., 2021).

1068 The multiple-step transport mechanisms can lead to varying carbon storage locations,

1069 affecting the sequestration potential of these systems. Additionally, resuspension and

1070 redistribution of sediments, especially during high-energy events, may expose

1071 previously buried organic material, leading to carbon remineralization and influencing

1072 coastal nutrient cycles and ecosystem health (Ståhlberg et al., 2006; Moriarty et al.,

1073 2018). Therefore, understanding these patterns is crucial for assessing the broader

1074 impacts on carbon cycling and coastal biogeochemical processes.

1075 **4.3 Limitations and future work**

1076   This study focuses on analyzing simulation results from a typical year,

1077 encompassing both wet and dry seasons from 2017 to 2018, to understand the

1078 seasonal variations and annual patterns of suspension, transport, and deposition of

1079 sediment in the PRE and adjacent shelf. However, it's essential to recognize that the

1080 long-term sediment transport and deposition dynamics in the Pearl River are

1081 influenced by numerous complex factors. These include changes in sea level and

1082 coastal line (Church and White, 2006; Harff et al., 2010; Hong et al., 2020; Lin et al.,

1083 2022; Ma et al., 2023), alterations in wind field and precipitation (Ning and Qian,

1084 2009; Young et al., 2011), natural sedimentation within the Pearl River Delta (Wu et

1085 al., 2010), modifications in sediment load and underwater volume of the estuary

1086 caused by anthropogenic impact (Wu et al., 2014; Wu et al., 2018; Lin et al., 2022),

1087 interannual variations of the shelf circulations (Liu et al., 2020; Deng et al., 2022) and

1088 Kuroshio intrusions (Caruso et al., 2006; Nan et al., 2015; Sun et al., 2020). Therefore,

1089 while this study sheds light on seasonal and annual timescale patterns, it cannot fully

1090 represent the short or long-term transport and deposition trends of the Pearl River

1091 sediment. Yet for many shelf systems, a lot of sediment transport happens during

1092 short-lived events such as hurricanes (Xu et al., 2016; Warner et al., 2017; Georgiou et

1093 al., 2024). Consideration of the episodicity of transport would be helpful for future

1094 studies (Xu et al., 2016; Warner et al., 2017; Georgiou et al., 2024).

1095   Additionally, it's important to note that this article primarily focuses on the fate of

1096 the Pearl River sediment on the inner shelf. However, within the expansion range of

1097 the Pearl River buoyant plume, a number of smaller rivers, including the Jiulong

1098 River, Han River, Moyang River, Jian River, Nanliu River, Changhua River and

1099 Nandu River, also contribute freshwater and sediment to the northern South China Sea

1100 (Milliman and Farnsworth, 2011; Zhang et al., 2012; Liu et al., 2016). Although these

1101 rivers contribute significantly less freshwater and sediment compared to the Pearl

1102 River, they still impact seawater salinity, suspended sediment concentration, and

1103 seabed geomorphology (Liu et al., 2016; Wang et al., 2023; Zong et al., 2024). Since

1104 the 1950s, South China delivers approximately 102 Mt/year of fluvial sediment to the

1105 SCS, with the Pearl River alone accounting for 84.3 Mt/year—about 83% of the total

1106 sediment load (Milliman and Farnsworth, 2011; Zhang et al., 2012; Liu et al., 2016).

1107 ~~The specific contributions of each river are detailed in Table 3.~~ While the ~~data~~

1108 ~~highlight the~~ Pearl River~~'s~~ plays a dominant role in sediment delivery to the northern

1109 South China Sea, a comprehensive understanding of the region's sedimentary

1110 processes and impacts ~~in the northern South China Sea~~ also requires a systematic

1111 investigation of the contributions from~~into the roles of the~~ smaller ~~contributing~~ rivers.

1112

1113 ~~**Table 3.** Annual mean runoff and annual suspended sediment load of major rivers in~~

1114 ~~South China that flow directly into the northern South China Sea since the 1950s~~

1115 ~~(Milliman and Farnsworth, 2011; Zhang et al., 2012; Liu et al., 2016).~~

~~River name~~	~~Runoff ($m^3 s^{-1}$)~~	~~Suspended sediment load (Mt/year)~~
~~Pearl River~~	~~9075~~	~~84.3~~
~~Jiulong River~~	~~476~~	~~3.1~~
~~Han River~~	~~825~~	~~10~~
~~Moyang River~~	~~269~~	~~0.8~~

~~Jian River~~	~~174~~	~~1.5~~
~~Nanliu River~~	~~162~~	~~1.1~~
~~Changhua River~~	~~120~~	~~0.08~~
~~Nandu River~~	~~179~~	~~0.4~~

1116

1117 Then, while the model used in this study performs well in~~has shown good~~

1118 validation ~~results~~, further progress relies on additional observational data to better

1119 constrain key parameters such as settling velocity and critical shear stress for erosion.

1120 ~~conducting more sensitivity experiments on sediment parameters, such as settling~~

1121 ~~velocity and critical shear stress for erosion, would be beneficial.~~ Direct

1122 measurements under varying conditions would help refine these inputs and improve

1123 model accuracy. For instance, ~~Settling~~ settling velocity ~~can~~ influences the location of

1124 sediment depocenters, with higher settling velocities leading to more proximal

1125 entrapment and vice versa (Harris et al., 2008). Similarly, critical erosion stress ~~can~~

1126 affects ~~the~~ sediment resuspension ~~of deposited sediment~~, particularly~~with higher~~

1127 ~~critical erosion stress resulting in less resuspension and more deposition especially~~

1128 during neap tides and weak wind wave events (Dong et al., 2020; Choi et al., 2023).

1129 Targeted~~Conducting such~~ sensitivity analyses, supported by such data, would enhance

1130 our understanding of sediment dynamics in estuaries and shelves. Besides, the model

1131 does not account for cohesive processes, such as consolidation and flocculation,

1132 which can significantly impact sediment behavior (Sherwood et al., 2018). Our model

1133 does not incorporate wave and current-supported gravity flows, which are important

1134 factors influencing sediment transport in submarine canyon areas (Harris et al., 2005;

1135 Ma et al., 2010; Zhang et al., 2020). Since our study area primarily focuses on the

1136 continental shelf and the simulated results indicate that sediment transport occurs

1137 mainly in the shallow inner shelf, where canyons are relatively rare, this omission has

1138 a relatively minor impact on our results.

1139 Lastly, we employ the COAWST model~~, which uses~~ with an S-coordinate vertical

1140 system ~~in the vertical direction~~ ~~with~~ that enhances ~~increased~~ resolution near the

1141 surface and bottom layers (Song and Haidvogel, 1994). This vertical layering allows

1142 cell heights to vary, enabling finer resolution in dynamically important regions and

1143 improving performance in areas with sloping bathymetry compared to traditional

1144 sigma-coordinate systems (Bryan, 1969; Song and Haidvogel, 1994). ~~In addition, our~~

1145 ~~model includes h~~Horizontal grid refinement in the PRE further enhances ~~, enhancing~~

1146 the model's ~~its~~ ability to resolve estuarine features, successfully capturing~~. As a result,~~

1147 ~~the model effectively captures~~ estuarine turbidity maxima (ETM) and ~~horizontal~~

1148 salinity fronts (Figures S11 and S12, see Supplement)~~. During summer, multiple~~

1149 ~~ETMs appear near the estuary bottom (Figure S11b), and while these features persist~~

1150 ~~in winter, their concentrations vary (Figure S12b)~~, consistent with the findings of

1151 Wang et al. (2018), Zhan et al. (2019), Zhang et al. (2021), Ma et al. (2022), and Ma

1152 et al. (2024). ~~Horizontal salinity fronts are also well represented, showing an upstream~~

1153 ~~shift from the high-discharge summer season to the low-discharge winter season~~

1154 ~~(Figures S11e–f and S12e–f), in agreement with previous studies by Zhang et al.~~

1155 ~~(2021) and Ma et al. (2024).~~ Nonetheless, compared with the S-coordinate system,

models that employ vertically adaptive layering (e.g., SCHISM, the Semi-implicit Cross-scale Hydroscience Integrated System Model, Zhang et al. (2016)) or Cartesian vertical coordinates (e.g., MITgcm, the MIT General Circulation Model, Marshall et al. (1997a); Marshall et al. (1997b)) generally perform better in regions with steep topographic gradients (Bijvelds, 2001). Future studies~~Therefore, future research~~ could benefit from such approaches combined with finer~~adopting models with higher~~ horizontal resolution and Cartesian vertical coordinates to improve ~~the simulation of~~ Pearl River-derived sediment dynamics simulations~~across the estuary and the adjacent shelf~~.

5. Conclusions

This study utilizes the COAWST model to quantitatively analyze the seasonal suspension, transport, and annual fate of Pearl River-derived sediment (classes 4-5 in Table 1) on the continental shelf over a typical year, capturing key marine variables such as water level, wave height, flow velocity, salinity, temperature, and SSC.

The monsoonal nature of the northern SCS (Figures 4a-b) induces pronounced seasonal variations in Pearl River-derived sediment transport and deposition (Figures 5 and 6). During the wet summer, calm conditions foster initial Pearl River-derived sediment deposition via the buoyant plume (Figures 5 and 7a). Conversely, winter's stronger winds and waves resuspend and transport Pearl River-derived sediments into "Gulf" region (Figures 6 and 7b). Our quantitative assessment reveals distinct spatial patterns in the annual fate of riverine sediments: approximately two-thirds of the Pearl

1178 River-derived sediment is retained within the estuarine vicinity ("Proximal" region),

1179 while about 9% reaches the continental shelf east of the PRE ("Eastern" and

1180 "Southeastern" regions), while similar proportions are transported to and retained in

1181 "Gulf" and "Distal" regions, respectively (Figure 7c). Furthermore, we evaluated the

1182 contributions of different physical drivers ~~processes~~ by comparing the Control run

1183 with the reduced-physics sensitivity experiments. Our analysis reveals distinct roles of

1184 tidal forces, wave action, and background circulation in governing the transport and

1185 deposition of Pearl River-derived sediments (Figures 8, 9, 11a-c, and 12a-c).

1186 Tidal dynamics play a primary role in ~~primarily~~ governing sediment behavior

1187 within and offshore of the PRE. In the presence of~~Relative to the Control run,~~

1188 ~~neglecting~~ tides, ~~leads to lower~~ bottom shear stress in the PRE is enhanced (Figures

1189 8a-b), promoting ~~higher~~ Pearl River-derived sediment resuspension and reducing

1190 excessive sediment deposition ~~deposition~~ in the PRE (Figure 11a), while

1191 facilitating~~and reduced~~ sediment retention patterns in "Gulf" and "Distal" regions

1192 (Figure 12a). Wave activity primarily controls Pearl River-derived sediment

1193 resuspension in three critical dimensions: (1) the river mouth, (2) the nearshore of

1194 "Eastern" and "Western" regions outside the estuary, and (3) periods characterized by

1195 high wave energy during winter (Figures 9c-d). ~~Excluding waves results in increased~~

1196 ~~modeled Pearl River-derived~~ These wave-driven resuspension processes regulate

1197 sediment deposition and accumulation patterns in these areas and seasons ~~times~~

1198 (Figure 11b), contributing to sediment export from the nearshore to offshore regions

1199 such as~~while reducing accumulation in~~ the "Gulf" ~~region~~ (Figure 11b). Background

circulation exerts its strongest influence~~is most influential~~ in summer (Figure 5a vs.

Figure 9e), with a strong northeastward current transporting Pearl River-derived

sediments to~~ward~~ regions "Eastern" and "Southeastern"~~③-④~~. When this current is

weak or absent, sediment delivery to these regions drops significantly, with only 0.84%

of the total reaching them, while deposition increases in the "Gulf" and "Distal"

regions ~~Without this current and under weak southerly winds, only 0.84% of Pearl~~

~~River-derived sediments are transported to regions ③-④, while deposition in "Gulf"~~

~~and "Distal" regions is greater compared to the Control run~~ (Figure 12c). The

sediment model solutions are also highly sensitive to the parameterization of sediment

characteristics and spin-up durations (riverine or seabed sediments) (Figures 10, 11d-f,

and 12d-f). The natural seasonal increase in critical shear stress for erosion during

winter counteracts part of the wave-enhanced resuspension capacity, thereby reducing

resuspension and erosion on the continental shelf east of the Leizhou Peninsula

(Figure 10b). ~~Neglecting the seasonal increase in critical shear stress for erosion leads~~

~~to enhanced resuspension and erosion in regions ①-⑥ during winter (Figure 10b),~~

~~which in turn shifts more sediment toward "Gulf" and "Distal" regions compared to~~

~~the Control run (Figure 12d).~~ Increasing the settling velocity reduces the overall

riverine SSC (Figures 10c-d) and results in a spatial redistribution pattern

characterized by greater retention mainly in "Proximal" and "Western" ~~in ①-③ and~~

~~⑤~~ regions and reduced riverine sediment presence in "Gulf", ~~and~~ "Distal" and

"Southeastern" regions relative to the Control simulation (Figure 12e). Additionally,

the modeled riverine SSC is influenced by pre-existing Pearl River–derived sediments,

as shown in the Cycle experiment (Figure 10e-f). The experiment highlights the effect of riverine sediment spin-up, showing that first-year retained Pearl River–derived sediments are predominantly redistributed from the "Gulf" region toward the more distant "Distal" region during the second year. ~~In contrast, the model exhibits only minor sensitivity to the duration of seabed sediment spin-up, as demonstrated in the Cycle2 experiment (see Supplement), in which riverine sediments present during the spin-up period were added to seabed sediment classes 1-2 at the start of the Cycle2.~~

Acknowledgments

This research was funded by the National Natural Science Foundation of China (grant numbers 42306015 and 42276169), the China Postdoctoral Science Foundation (grant number 2023M743988). Wenping Gong is supported by the Southern Marine Science and Engineering Guangdong Laboratory (Zhuhai) (SML2023SP238). The authors would like to thank the crew of the R/V Changhe Ocean for their valuable contribution during the collection of the field data. We express our gratitude to the Co-editors-in-chief, Dr. Mario Hoppema, and three anonymous reviewers for their valuable suggestions in enhancing and improving this article.

Data availability

The figure data and model configuration files used in this paper can be downloaded from: https://doi.org/10.5281/zenodo.15013448. The HYbrid Coordinate Ocean Model (HYCOM) outputs are from: http://hycom.org/hycom. The NCEP Climate Forecast System Version 2 (CFSv2) reanalysis data can be obtained at the following website: https://rda.ucar.edu/datasets/ds094.1/dataaccess/. The NOAA

WAVEWATCH III global ocean wave model output fields can be downloaded from: ftp://polar.ncep.noaa.gov/pub/history/waves. Hourly water-level data observed at Quarry Bay station are provided by the Hong Kong Observatory website: https://www.hko.gov.hk/sc/tide/marine/realtide.htm?s=QUB&t=TABLE. Hourly water-level data from Zhapo and Qinglan stations, provided by the Flanders Marine Institute (VLIZ), are part of the UNESCO/IOC Global Sea Level Observing System (GLOSS) and accessible at http://www.ioc-sealevelmonitoring.org. The mooring data for the M1 and M2 stations are sourced from Liu et al. (2023) and Li et al. (2024a). ~~The figure data and model configuration files used in this paper can be downloaded from: https://doi.org/10.5281/zenodo.15013448.~~

Declaration of Competing interests

The authors declare that they have no known competing financial interests or personal relationships that could have appeared to influence the work reported in this paper.

CRediT authorship contribution statement

GZ: Conceptualization, Numerical modeling, Validation, Data visualization, Writing-original draft, and Funding acquisition. **SH:** Writing-review & editing, Validation. **XY:** Writing-review & editing. **HZ:** Writing-review & editing. **WG:** Writing-review & editing, and Funding acquisition

Supplement:

The Supplement includes validation and analysis of the model's water levels, Hsig, flow velocities, salinity, temperature, and SSC. It provides additional text and

1266 figures that support the model validation and supplementary analyses, which could

1267 not be fully presented in the main article due to space limitations.

References

1269 Bever, A. J., Harris, C. K., Sherwood, C. R., and Signell, R. P.: Deposition and flux of sediment from

1270   the Po River, Italy: An idealized and wintertime numerical modeling study, Marine Geology, 260,

1271   69-80, 10.1016/j.margeo.2009.01.007, 2009.

1272 Bever, A. J., and MacWilliams, M. L.: Simulating sediment transport processes in San Pablo Bay using

1273   coupled hydrodynamic, wave, and sediment transport models, Marine Geology, 345, 235-253,

1274   10.1016/j.margeo.2013.06.012, 2013.

1275 Bian, C., Jiang, W., and Greatbatch, R. J.: An exploratory model study of sediment transport sources

1276   and deposits in the Bohai Sea, Yellow Sea, and East China Sea, Journal of Geophysical Research:

1277   Oceans, 118, 5908-5923, https://doi.org/10.1002/2013JC009116, 2013.

1278 Bijvelds, M. D. J. P.: Numerical modelling of estuarine flow over steep topography, Doctoral, Delft

1279   University of Technology, 2001.

1280 Booij, N., Ris, R. C., and Holthuijsen, L. H.: A third-generation wave model for coastal regions: 1.

1281   Model description and validation, Journal of Geophysical Research: Oceans, 104, 7649-7666,

1282   https://doi.org/10.1029/98JC02622, 1999.

1283 Brand, A., Lacy, J. R., Hsu, K., Hoover, D., Gladding, S., and Stacey, M. T.: Wind-enhanced

1284   resuspension in the shallow waters of South San Francisco Bay: Mechanisms and potential

1285   implications for cohesive sediment transport, Journal of Geophysical Research, 115,

1286   10.1029/2010jc006172, 2010.

1287 Briggs, K. B., Cartwright, G., Friedrichs, C. T., and Shivarudruppa, S.: Biogenic effects on cohesive

1288   sediment erodibility resulting from recurring seasonal hypoxia on the Louisiana shelf, Continental

1289   Shelf Research, 93, 17-26, https://doi.org/10.1016/j.csr.2014.11.005, 2015.

1290 Bryan, K.: A numerical method for the study of the circulation of the world ocean, Journal of

1291   Computational Physics, 4, 347-376, https://doi.org/10.1016/0021-9991(69)90004-7, 1969.

1292 Burchard, H., Schuttelaars, H. M., and Ralston, D. K.: Sediment Trapping in Estuaries, Annual Review

1293   of Marine Science, 10, 371-395, 10.1146/annurev-marine-010816-060535, 2018.

Cao, L., Liu, J., Shi, X., He, W., and Chen, Z.: Source-to-sink processes of fluvial sediments in the northern South China Sea: Constraints from river sediments in the coastal region of South China, Journal of Asian Earth Sciences, 185, 104020, 10.1016/j.jseaes.2019.104020, 2019.

Cao, Z., Ren, J., Deng, Z., Ye, L., and Wu, J.: Small-scale spatial variability in erosion threshold and bedform for cohesive sediment measured by 3D Sonar, Journal of Hydrology, 650, 132513, 10.1016/j.jhydrol.2024.132513, 2025.

Caruso, M. J., Gawarkiewicz, G. G., and Beardsley, R. C.: Interannual variability of the Kuroshio intrusion in the South China Sea, Journal of Oceanography, 62, 559-575, 10.1007/s10872-006-0076-0, 2006.

Chapman, D. C.: Numerical Treatment of Cross-Shelf Open Boundaries in a Barotropic Coastal Ocean Model, Journal of Physical Oceanography, 15, 1060-1075, 1985.

Charnock, H.: Wind stress on a water surface, Quarterly Journal of the Royal Meteorological Society, 81, 639-640, https://doi.org/10.1002/qj.49708135027, 1955.

Chassignet, E. P., Hurlburt, H. E., Smedstad, O. M., Halliwell, G. R., Hogan, P. J., Wallcraft, A. J., Baraille, R., and Bleck, R.: The HYCOM (HYbrid Coordinate Ocean Model) data assimilative system, Journal of Marine Systems, 65, 60-83, https://doi.org/10.1016/j.jmarsys.2005.09.016, 2007.

Chen, S.-N., Geyer, W. R., Sherwood, C. R., and Ralston, D. K.: Sediment transport and deposition on a river-dominated tidal flat: An idealized model study, Journal of Geophysical Research, 115, 10.1029/2010jc006248, 2010.

Chen, Y., Deng, B., Saito, Y., Wang, Z., Yang, X., and Wu, J.: Pearl River sediment dispersal over its associated delta–estuary–shelf system during the Holocene, Sedimentology, 70, 2331-2354, 10.1111/sed.13123, 2023.

Chen, Z., Pan, J., and Jiang, Y.: Role of pulsed winds on detachment of low salinity water from the Pearl River Plume Upwelling and mixing processes, Journal of Geophysical Research: Oceans, 121, 2769-2788, 10.1002/2015JC011337, 2016.

Chen, Z., Gong, W., Cai, H., Chen, Y., and Zhang, H.: Dispersal of the Pearl River plume over continental shelf in summer, Estuarine, Coastal and Shelf Science, 194, 252-262, 10.1016/j.ecss.2017.06.025, 2017a.

Chen, Z., Pan, J., Jiang, Y., and Lin, H.: Far-reaching transport of Pearl River plume water by upwelling jet in the northeastern South China Sea, Journal of Marine Systems, 173, 60-69, 10.1016/j.jmarsys.2017.04.008, 2017b.

Cheng, P., Li, M., and Li, Y.: Generation of an estuarine sediment plume by a tropical storm, Journal of Geophysical Research: Oceans, 118, 856-868, 10.1002/jgrc.20070, 2013.

Choi, S. M., Seo, J. Y., and Ha, H. K.: Contribution of local erosion enhanced by winds to sediment transport in intertidal flat, Marine Geology, 465, 107171, 10.1016/j.margeo.2023.107171, 2023.

Church, J. A., and White, N. J.: A 20th century acceleration in global sea-level rise, Geophysical Research Letters, 33, n/a-n/a, 10.1029/2005gl024826, 2006.

Cui, Y., Wu, J., Ren, J., and Xu, J.: Physical dynamics structures and oxygen budget of summer hypoxia in the Pearl River Estuary, Limnology and Oceanography, 64, 131-148, 10.1002/lno.11025, 2018.

Cui, Y., Wu, J., Tan, E., and Kao, S. J.: Role of Particle Resuspension in Maintaining Hypoxic Level in the Pearl River Estuary, Journal of Geophysical Research: Oceans, 127, 10.1029/2021jc018166, 2022.

Dai, S. B., Yang, S. L., and Cai, A. M.: Impacts of dams on the sediment flux of the Pearl River, southern China, Catena, 76, 36-43, 10.1016/j.catena.2008.08.004, 2008.

Dalyander, P. S., Butman, B., Sherwood, C. R., Signell, R. P., and Wilkin, J. L.: Characterizing wave- and current- induced bottom shear stress: U.S. middle Atlantic continental shelf, Continental Shelf Research, 52, 73-86, https://doi.org/10.1016/j.csr.2012.10.012, 2013.

Deng, Y., Liu, Z., Zu, T., Hu, J., Gan, J., Lin, Y., Li, Z., Quan, Q., and Cai, Z.: Climatic Controls on the Interannual Variability of Shelf Circulation in the Northern South China Sea, Journal of Geophysical Research: Oceans, 127, e2022JC018419, https://doi.org/10.1029/2022JC018419, 2022.

Dong, H., Jia, L., He, Z., Yu, M., and Shi, Y.: Application of parameters and paradigms of the erosion and deposition for cohesive sediment transport modelling in the Lingdingyang Estuary, China, Applied Ocean Research, 94, 101999, 10.1016/j.apor.2019.101999, 2020.

Dong, L., Su, J., Wong, L., Cao, Z., and Chen, J.: Seasonal variation and dynamics of the Pearl River plume, Continental Shelf Research, 24, 1761-1777, 10.1016/j.csr.2004.06.006, 2004.

1352 Egbert, G. D., and Erofeeva, S. Y.: Efficient inverse Modeling of barotropic ocean tides, Journal of
1353   Atmospheric and Oceanic Technology, 19, 183-204, Doi
1354   10.1175/1520-0426(2002)019<0183:Eimobo>2.0.Co;2, 2002.

1355 Eidam, E. F., Nittrouer, C. A., Ogston, A. S., DeMaster, D. J., Liu, J. P., Nguyen, T. T., and Nguyen, T.
1356   N.: Dynamic controls on shallow clinoform geometry: Mekong Delta, Vietnam, Continental Shelf
1357   Research, 147, 165-181, 10.1016/j.csr.2017.06.001, 2017.

1358 Fairall, C. W., Bradley, E. F., Rogers, D. P., Edson, J. B., and Young, G. S.: Bulk parameterization of
1359   air-sea fluxes for Tropical Ocean-Global Atmosphere Coupled-Ocean Atmosphere Response
1360   Experiment, Journal of Geophysical Research: Oceans, 101, 3747-3764,
1361   https://doi.org/10.1029/95JC03205, 1996.

1362 Flather, R. A.: A tidal model of the north-west European continental shelf, Memoires Societe Royale
1363   des Sciences de Liege, 10, 141-164, 1976.

1364 Fox, J. M., Hill, P. S., Milligan, T. G., Ogston, A. S., and Boldrin, A.: Floc fraction in the waters of the
1365   Po River prodelta, Continental Shelf Research, 24, 1699-1715,
1366   https://doi.org/10.1016/j.csr.2004.05.009, 2004.

1367 Gan, J., Cheung, A., Guo, X., and Li, L.: Intensified upwelling over a widened shelf in the northeastern
1368   South China Sea, Journal of Geophysical Research, 114, 10.1029/2007jc004660, 2009.

1369 Gan, J., San Ho, H., and Liang, L.: Dynamics of Intensified Downwelling Circulation over a Widened
1370   Shelf in the Northeastern South China Sea, Journal of Physical Oceanography, 43, 80-94,
1371   10.1175/jpo-d-12-02.1, 2013.

1372 Gao, S., and Collins, M. B.: Holocene sedimentary systems on continental shelves, Marine Geology,
1373   352, 268-294, 10.1016/j.margeo.2014.03.021, 2014.

1374 Gao, X., Chen, S., Xie, X., Long, A., and Ma, F.: Non-aromatic hydrocarbons in surface sediments near
1375   the Pearl River estuary in the South China Sea, Environmental Pollution, 148, 40-47,
1376   10.1016/j.envpol.2006.11.001, 2007.

1377 Gao, X., Arthur Chen, C.-T., Wang, G., Xue, Q., Tang, C., and Chen, S.: Environmental status of Daya
1378   Bay surface sediments inferred from a sequential extraction technique, Estuarine, Coastal and
1379   Shelf Science, 86, 369-378, 10.1016/j.ecss.2009.10.012, 2010.

1380 Ge, Q., Liu, J. P., Xue, Z., and Chu, F.: Dispersal of the Zhujiang River (Pearl River) derived sediment

1381   in the Holocene, Acta Oceanologica Sinica, 33, 1-9, 10.1007/s13131-014-0407-8, 2014.

1382   Ge, Q., Xue, Z., Yao, Z., Zang, Z., and Chu, F.: Anti-phase relationship between the East Asian winter

1383   monsoon and summer monsoon during the Holocene?, Journal of Ocean University of China, 16,

1384   175-183, 10.1007/s11802-017-3098-x, 2017.

1385   Ge, Q., Xu, D., Ye, L., Yang, K., and Yao, Z.: Linking Monsoon Activity with River-Derived Sediments

1386   Deposition in the Northern South China Sea, Journal of Ocean University of China, 18, 1098-1104,

1387   10.1007/s11802-019-4155-4, 2019.

1388   Georgiou, I. Y., FitzGerald, D. M., Sakib, M. M., Messina, F., Kulp, M. A., and Miner, M. D.: Storm

1389   Dynamics Control Sedimentation and Shelf-Bay-Marsh Sediment Exchange Along the Louisiana

1390   Coast, Geophysical Research Letters, 51, e2024GL111344,

1391   https://doi.org/10.1029/2024GL111344, 2024.

1392   Geyer, W. R., Hill, P. S., and Kineke, G. C.: The transport, transformation and dispersal of sediment by

1393   buoyant coastal flows, Continental Shelf Research, 24, 927-949, 10.1016/j.csr.2004.02.006, 2004.

1394   Gong, W., Chen, Y., Zhang, H., and Chen, Z.: Effects of Wave–Current Interaction on Salt Intrusion

1395   During a Typhoon Event in a Highly Stratified Estuary, Estuaries and Coasts, 41, 1904-1923,

1396   10.1007/s12237-018-0393-8, 2018a.

1397   Gong, W., Lin, Z., Chen, Y., Chen, Z., Shen, J., and Zhang, H.: Effect of waves on the dispersal of the

1398   Pearl River plume in winter, Journal of Marine Systems, 186, 47-67,

1399   10.1016/j.jmarsys.2018.05.003, 2018b.

1400   Haidvogel, D. B., Arango, H., Budgell, W. P., Cornuelle, B. D., Curchitser, E., Di, L. E., Fennel, K.,

1401   Geyer, W. R., Hermann, A. J., Lanerolle, L., Levin, J., McWilliams, J. C., Miller, A. J., Moore, A.

1402   M., Powell, T. M., Shchepetkin, A. F., Sherwood, C. R., Signell, R. P., Warner, J. C., and Wilkin, J.:

1403   Ocean forecasting in terrain-following coordinates: Formulation and skill assessment of the

1404   Regional Ocean Modeling System, Journal of Computational Physics, 227, 3595-3624,

1405   10.1016/j.jcp.2007.06.016, 2008.

1406   Hanebuth, T. J. J., Lantzsch, H., and Nizou, J.: Mud depocenters on continental shelves—appearance,

1407   initiation times, and growth dynamics, Geo-Marine Letters, 35, 487-503,

1408   10.1007/s00367-015-0422-6, 2015.

1409   Harff, J., Leipe, T., and Zhou, D.: Pearl River Estuary related sediments as response to Holocene

climate change and anthropogenic impact (PECAI), Journal of Marine Systems, 82, S1-S2, 10.1016/j.jmarsys.2010.02.008, 2010.

Harris, C. K., Traykovski, P. A., and Geyer, W. R.: Flood dispersal and deposition by near-bed gravitational sediment flows and oceanographic transport: A numerical modeling study of the Eel River shelf, northern California, Journal of Geophysical Research: Oceans, 110, 10.1029/2004jc002727, 2005.

Harris, C. K., Sherwood, C. R., Signell, R. P., Bever, A. J., and Warner, J. C.: Sediment dispersal in the northwestern Adriatic Sea, Journal of Geophysical Research, 113, 10.1029/2006jc003868, 2008.

Hong, B., Liu, Z., Shen, J., Wu, H., Gong, W., Xu, H., and Wang, D.: Potential physical impacts of sea-level rise on the Pearl River Estuary, China, Journal of Marine Systems, 201, 103245, 10.1016/j.jmarsys.2019.103245, 2020.

Hu, J., Li, S., and Geng, B.: Modeling the mass flux budgets of water and suspended sediments for the river network and estuary in the Pearl River Delta, China, Journal of Marine Systems, 88, 252-266, 10.1016/j.jmarsys.2011.05.002, 2011.

Hu, S., Li, Y., Hu, P., Zhang, H., Zhang, G., and Gong, W.: The Impacts of Far-Field Typhoon-Generated Coastal Trapped Waves on the Hydrodynamics in the Northern South China Sea: A Case Study of Typhoon In - Fa, Journal of Geophysical Research: Oceans, 129, 10.1029/2024jc021359, 2024.

Huang, D., Du, J., Deng, B., and Zhang, J.: Distribution patterns of particle-reactive radionuclides in sediments off eastern Hainan Island, China: Implications for source and transport pathways, Continental Shelf Research, 57, 10-17, 10.1016/j.csr.2012.04.019, 2013.

Jacob, R., Larson, J., and Ong, E.: M × N Communication and Parallel Interpolation in Community Climate System Model Version 3 Using the Model Coupling Toolkit, IJHPCA, 19, 293-307, 10.1177/1094342005056116, 2005.

Kirby, M. F., Devoy, B., Law, R. J., Ward, A., and Aldridge, J.: The use of a bioassay based approach to the hazard/risk assessment of cargo derived toxicity during shipping accidents: a case study--the MSC Napoli, Marine Pollution Bulletin, 56, 781-786, 10.1016/j.marpolbul.2008.01.006, 2008.

Krige, D. G.: A Statistical Approach to Some Basic Mine Valuation Problems on the Witwatersrand,

Chemical, Metallurgical and Mining Society of South Africa, 1951.

Kuehl, S. A., Alexander, C. R., Blair, N. E., Harris, C. K., Marsaglia, K. M., Ogston, A. S., Orpin, A. R., Roering, J. J., Bever, A. J., Bilderback, E. L., Carter, L., Cerovski-Darriau, C., Childress, L. B., Reide Corbett, D., Hale, R. P., Leithold, E. L., Litchfield, N., Moriarty, J. M., Page, M. J., Pierce, L. E. R., Upton, P., and Walsh, J. P.: A source-to-sink perspective of the Waipaoa River margin, Earth-Science Reviews, 153, 301-334, 10.1016/j.earscirev.2015.10.001, 2016.

Kumar, N., Voulgaris, G., Warner, J. C., and Olabarrieta, M.: Implementation of the vortex force formalism in the coupled ocean-atmosphere-wave-sediment transport (COAWST) modeling system for inner shelf and surf zone applications, Ocean Modelling, 47, 65-95, 10.1016/j.ocemod.2012.01.003, 2012.

LaRowe, D. E., Arndt, S., Bradley, J. A., Estes, E. R., Hoarfrost, A., Lang, S. Q., Lloyd, K. G., Mahmoudi, N., Orsi, W. D., Shah Walter, S. R., Steen, A. D., and Zhao, R.: The fate of organic carbon in marine sediments - New insights from recent data and analysis, Earth-Science Reviews, 204, 103146, 10.1016/j.earscirev.2020.103146, 2020.

Larson, J., Jacob, R., and Ong, E.: The Model Coupling Toolkit: A New Fortran90 Toolkit for Building Multiphysics Parallel Coupled Models, IJHPCA, 19, 277-292, 2005.

Li, J., Li, M., and Xie, L.: Observations of near-inertial oscillations trapped at inclined front on continental shelf of the northwestern South China Sea, EGUsphere, 2024, 1-25, 10.5194/egusphere-2024-3909, 2024a.

Li, X., Chrysagi, E., Klingbeil, K., and Burchard, H.: Impact of Islands on Tidally Dominated River Plumes: A High-Resolution Modeling Study, Journal of Geophysical Research: Oceans, 129, e2023JC020272, https://doi.org/10.1029/2023JC020272, 2024b.

Lin, S., Niu, J., Liu, G., Wei, X., and Cai, S.: Variations of suspended sediment transport caused by changes in shoreline and bathymetry in the Zhujiang (Pearl) River Estuary in the wet season, Acta Oceanologica Sinica, 41, 54-73, 10.1007/s13131-022-2017-1, 2022.

Lin, W., Feng, Y., Yu, K., Lan, W., Wang, Y., Mo, Z., Ning, Q., Feng, L., He, X., and Huang, Y.: Long-lived radionuclides in marine sediments from the Beibu Gulf, South China Sea: Spatial distribution, controlling factors, and proxy for transport pathway, Marine Geology, 424, 106157, 10.1016/j.margeo.2020.106157, 2020.

1467   Liu, G., and Cai, S.: Modeling of suspended sediment by coupled wave-current model in the Zhujiang

1468   (Pearl) River Estuary, Acta Oceanologica Sinica, 38, 22-35, 10.1007/s13131-019-1455-3, 2019.

1469   Liu, H., Ye, L., Zhou, W., and Wu, J.: Salt-wedge intrusion-retreat cycle induced sediment floc

1470   dynamics in bottom boundary layer (BBL) of a micro-tidal estuary, Marine Geology, 466, 107175,

1471   10.1016/j.margeo.2023.107175, 2023.

1472   Liu, J. P., Xue, Z., Ross, K., Yang, Z., and Gao, S.: Fate of Sediments Delivered to the Sea by Asian

1473   Large Rivers: Long-Distance Transport and Formation of Remote Alongshore Clinothems,

1474   Sediment. Rec., 7, 10.2110/sedred.2009.4.4, 2009.

1475   Liu, N., Geng, B., Xue, H., Xiu, P., Wang, Q., and Wang, D.: Interannual Variability of Shelf and Slope

1476   Circulations in the Northern South China Sea, Journal of Ocean University of China, 19,

1477   1005-1016, 10.1007/s11802-020-4446-9, 2020.

1478   Liu, Y., Gao, S., Wang, Y. P., Yang, Y., Long, J., Zhang, Y., and Wu, X.: Distal mud deposits associated

1479   with the Pearl River over the northwestern continental shelf of the South China Sea, Marine

1480   Geology, 347, 43-57, 10.1016/j.margeo.2013.10.012, 2014.

1481   Liu, Z., Zhao, Y., Colin, C., Stattegger, K., Wiesner, M. G., Huh, C.-A., Zhang, Y., Li, X.,

1482   Sompongchaiyakul, P., You, C.-F., Huang, C.-Y., Liu, J. T., Siringan, F. P., Le, K. P., Sathiamurthy,

1483   E., Hantoro, W. S., Liu, J., Tuo, S., Zhao, S., Zhou, S., He, Z., Wang, Y., Bunsomboonsakul, S.,

1484   and Li, Y.: Source-to-sink transport processes of fluvial sediments in the South China Sea,

1485   Earth-Science Reviews, 153, 238-273, 10.1016/j.earscirev.2015.08.005, 2016.

1486   Lu, X., Wang, Z., Guo, X., Gu, Y., Liang, W., and Liu, L.: Impacts of metal contamination and

1487   eutrophication on dinoflagellate cyst assemblages along the Guangdong coast of southern China,

1488   Marine Pollution Bulletin, 120, 239-249, 10.1016/j.marpolbul.2017.05.032, 2017.

1489   Ma, C., Zhao, J., Ai, B., Sun, S., and Yang, Z.: Machine Learning Based Long-Term Water Quality in

1490   the Turbid Pearl River Estuary, China, Journal of Geophysical Research: Oceans, 127,

1491   10.1029/2021jc018017, 2022.

1492   Ma, M., Zhang, W., Chen, W., Deng, J., and Schrum, C.: Impacts of morphological change and

1493   sea-level rise on stratification in the Pearl River Estuary, Frontiers in Marine Science, Volume 10 -

1494   2023, 10.3389/fmars.2023.1072080, 2023.

1495   Ma, M., Porz, L., Schrum, C., and Zhang, W.: Physical mechanisms, dynamics and interconnections of

multiple estuarine turbidity maximum in the Pearl River estuary, Frontiers in Marine Science, Volume 11 - 2024, 10.3389/fmars.2024.1385382, 2024.

Ma, Y., Friedrichs, C. T., Harris, C. K., and Wright, L. D.: Deposition by seasonal wave- and current-supported sediment gravity flows interacting with spatially varying bathymetry: Waiapu shelf, New Zealand, Marine Geology, 275, 199-211, https://doi.org/10.1016/j.margeo.2010.06.001, 2010.

Madsen, O. S.: Spectral Wave-Current Bottom Boundary Layer Flows, Coastal Engineering 1, 384-398, 1994.

Mao, Q., Shi, P., Yin, K., Gan, J., and Qi, Y.: Tides and tidal currents in the Pearl River Estuary, Continental Shelf Research, 24, 1797-1808, 10.1016/j.csr.2004.06.008, 2004.

Marshall, J., Adcroft, A., Hill, C., Perelman, L., and Heisey, C.: A finite-volume, incompressible Navier Stokes model for studies of the ocean on parallel computers, Journal of Geophysical Research: Oceans, 102, 5753-5766, https://doi.org/10.1029/96JC02775, 1997a.

Marshall, J., Hill, C., Perelman, L., and Adcroft, A.: Hydrostatic, quasi-hydrostatic, and nonhydrostatic ocean modeling, Journal of Geophysical Research: Oceans, 102, 5733-5752, https://doi.org/10.1029/96JC02776, 1997b.

McKee, B. A., Aller, R. C., Allison, M. A., Bianchi, T. S., and Kineke, G. C.: Transport and transformation of dissolved and particulate materials on continental margins influenced by major rivers: benthic boundary layer and seabed processes, Continental Shelf Research, 24, 899-926, https://doi.org/10.1016/j.csr.2004.02.009, 2004.

McWilliams, J. C., Restrepo, J. M., and Lane, E. M.: An asymptotic theory for the interaction of waves and currents in coastal waters, Journal of Fluid Mechanics, 511, 135-178, 10.1017/s0022112004009358, 2004.

Meade, R. H.: Landward Transport of Bottom Sediments in Estuaries of the Atlantic Coastal Plain, Journal of Sedimentary Petrology, 39, 222-234, 1969.

Milliman, J., and Farnsworth, K. L.: River discharge to the coastal ocean: A global synthesis. UK: Cambridge University Press; ISBN 978-0-521-87987-3, 2011.

Ministry of Water Resources of the PRC. 2022. Bulletin of River Sediment in China. http://www.mwr.gov.cn/sj/#tjgb.

Moriarty, J. M., Harris, C. K., Friedrichs, M. A. M., Fennel, K., and Xu, K.: Impact of Seabed Resuspension on Oxygen and Nitrogen Dynamics in the Northern Gulf of Mexico: A Numerical Modeling Study, Journal of Geophysical Research: Oceans, 123, 7237-7263, https://doi.org/10.1029/2018JC013950, 2018.

Nan, F., Xue, H., and Yu, F.: Kuroshio intrusion into the South China Sea: A review, Progress in Oceanography, 137, 314-333, https://doi.org/10.1016/j.pocean.2014.05.012, 2015.

Ning, L., and Qian, Y.: Interdecadal change in extreme precipitation over South China and its mechanism, Advances in Atmospheric Sciences, 26, 109-118, 10.1007/s00376-009-0109-x, 2009.

Nittrouer, C. A., and Wright, L. D.: Transport of particles across continental shelves, Reviews of Geophysics, 32, 85-113, https://doi.org/10.1029/93RG02603, 1994.

Orlanski, I.: A simple boundary condition for unbounded hyperbolic flows, Journal of Computational Physics, 21, 251-269, 10.1016/0021-9991(76)90023-1, 1976.

Ou, S., Zhang, H., and Wang, D.: Dynamics of the buoyant plume off the Pearl River Estuary in summer, Environmental Fluid Mechanics, 9, 471-492, 10.1007/s10652-009-9146-3, 2009.

Ralston, D. K., Geyer, W. R., and Warner, J. C.: Bathymetric controls on sediment transport in the Hudson River estuary: Lateral asymmetry and frontal trapping, Journal of Geophysical Research: Oceans, 117, 10.1029/2012jc008124, 2012.

Ralston, D. K., and Geyer, W. R.: Sediment Transport Time Scales and Trapping Efficiency in a Tidal River, Journal of Geophysical Research: Earth Surface, 122, 2042-2063, 10.1002/2017jf004337, 2017.

Raymond, W. H., and Kuo, H. L.: A radiation boundary condition for multi-dimensional flows, Quarterly Journal of the Royal Meteorological Society, 110, 535-551, 1984.

Repasch, M., Scheingross, J. S., Hovius, N., Lupker, M., Wittmann, H., Haghipour, N., Gröcke, D. R., Orfeo, O., Eglinton, T. I., and Sachse, D.: Fluvial organic carbon cycling regulated by sediment transit time and mineral protection, Nature Geoscience, 14, 842-848, 10.1038/s41561-021-00845-7, 2021.

Saha, S., Moorthi, S., Wu, X., Wang, J., Nadiga, S., Tripp, P., Behringer, D., Hou, Y.-T., Chuang, H.-y., Iredell, M., Ek, M., Meng, J., Yang, R., Mendez, M. P., van den Dool, H., Zhang, Q., Wang, W., Chen, M., and Becker, E.: The NCEP Climate Forecast System Version 2, Journal of Climate, 27,

2185-2208, https://doi.org/10.1175/JCLI-D-12-00823.1, 2014.

Sanford, L. P.: Wave-forced resuspension of upper Chesapeake Bay muds, Estuaries, 17, 148-165, 1994.

Shchepetkin, A. F., and McWilliams, J. C.: The regional oceanic modeling system (ROMS): a split-explicit, free-surface, topography-following-coordinate oceanic model, Ocean Modelling, 9, 347-404, https://doi.org/10.1016/j.ocemod.2004.08.002, 2005.

Shepard, F. P.: Nomenclature Based on Sand-silt-clay Ratios, Journal of Sedimentary Research, 24, 151-158, 1954.

Sherwood, C. R., Aretxabaleta, A. L., Harris, C. K., Rinehimer, J. P., Verney, R., and Ferré, B.: Cohesive and mixed sediment in the Regional Ocean Modeling System (ROMS v3.6) implemented in the Coupled Ocean–Atmosphere–Wave–Sediment Transport Modeling System (COAWST r1234), Geoscientific Model Development, 11, 1849-1871, 10.5194/gmd-11-1849-2018, 2018.

Shi, M., Chen, C., Xu, Q., Lin, H., Liu, G., Wang, H., Wang, F., and Yan, J.: The Role of Qiongzhou Strait in the Seasonal Variation of the South China Sea Circulation, Journal of Physical Oceanography, 32, 103-121, 2002.

Skamarock, W. C., Klemp, J. B., Dudhia, J., Gill, D. O., Barker, D. M., Wang, W., and Powers, J. G.: A Description of the Advanced Research WRF Version 2, 2005,

Smagorinsky, J.: GENERAL CIRCULATION EXPERIMENTS WITH THE PRIMITIVE EQUATIONS, Monthly Weather Review, 91, 99-164, 10.1175/1520-0493(1963)091<0099:gcewtp>2.3.co;2, 1963.

Song, Y., and Haidvogel, D.: A Semi-implicit Ocean Circulation Model Using a Generalized Topography-Following Coordinate System, Journal of Computational Physics, 115, 228-244, https://doi.org/10.1006/jcph.1994.1189, 1994.

Ståhlberg, C., Bastviken, D., Svensson, B. H., and Rahm, L.: Mineralisation of organic matter in coastal sediments at different frequency and duration of resuspension, Estuarine, Coastal and Shelf Science, 70, 317-325, https://doi.org/10.1016/j.ecss.2006.06.022, 2006.

Su, J.: Overview of the South China Sea circulation and its influence on the coastal physical oceanography outside the Pearl River Estuary, Continental Shelf Research, 24, 1745-1760,

1583   10.1016/j.csr.2004.06.005, 2004.

1584 Sun, Z., Zhang, Z., Qiu, B., Zhang, X., Zhou, C., Huang, X., Zhao, W., and Tian, J.: Three-Dimensional

1585   Structure and Interannual Variability of the Kuroshio Loop Current in the Northeastern South

1586   China Sea, Journal of Physical Oceanography, 50, 2437-2455,

1587   https://doi.org/10.1175/JPO-D-20-0058.1, 2020.

1588 Tolman, H., Accensi, M., Alves, J.-H., Ardhuin, F., Barbariol, F., Benetazzo, A., Bennis, A.-C., Bidlot,

1589   J., Booij, N., Boutin, G., Campbell, T., Chalikov, D., Chawla, A., Cheng, S., Collins Iii, C., Filipot,

1590   J.-F., Foreman, M., Janssen, P., Leckler, F., and Westhuysen, A.: User manual and system

1591   documentation of WAVEWATCH III (R) version 5.16, 2016.

1592 Turner, A., and Millward, G. E.: Suspended Particles: Their Role in Estuarine Biogeochemical Cycles,

1593   Estuarine, Coastal and Shelf Science, 55, 857-883, 10.1006/ecss.2002.1033, 2002.

1594 van der Wegen, M., Dastgheib, A., Jaffe, B. E., and Roelvink, D.: Bed composition generation for

1595   morphodynamic modeling: case study of San Pablo Bay in California, USA, Ocean Dynamics, 61,

1596   173-186, 10.1007/s10236-010-0314-2, 2010.

1597 Walsh, J. P., and Nittrouer, C. A.: Understanding fine-grained river-sediment dispersal on continental

1598   margins, Marine Geology, 263, 34-45, 10.1016/j.margeo.2009.03.016, 2009.

1599 Wang, C., Li, W., Chen, S., Li, D., Wang, D., and Liu, J.: The spatial and temporal variation of total

1600   suspended solid concentration in Pearl River Estuary during 1987-2015 based on remote sensing,

1601   Science of The Total Environment, 618, 1125-1138, 10.1016/j.scitotenv.2017.09.196, 2018.

1602 Wang, C., Liu, Z., Harris, C. K., Wu, X., Wang, H., Bian, C., Bi, N., Duan, H., and Xu, J.: The Impact

1603   of Winter Storms on Sediment Transport Through a Narrow Strait, Bohai, China, Journal of

1604   Geophysical Research: Oceans, 125, e2020JC016069, https://doi.org/10.1029/2020JC016069,

1605   2020.

1606 Wang, S., Zhang, N., Chen, H., Li, L., and Yan, W.: The surface sediment types and their rare earth

1607   element characteristics from the continental shelf of the northern south China sea, Continental

1608   Shelf Research, 88, 185-202, 10.1016/j.csr.2014.08.005, 2014.

1609 Wang, S., Wu, S., Yan, W., Huang, W., Miao, L., Lu, J., Chen, Z., and Liu, F.: Rare metal elements in

1610   surface sediment from five bays on the northeastern coast of the South China Sea, Environmental

1611   Earth Sciences, 74, 4961-4971, 10.1007/s12665-015-4504-6, 2015.

Wang, S., Li, J., Wu, S., Yan, W., Huang, W., Miao, L., and Chen, Z.: The distribution characteristics of rare metal elements in surface sediments from four coastal bays on the northwestern South China Sea, Estuarine, Coastal and Shelf Science, 169, 106-118, 10.1016/j.ecss.2015.12.001, 2016.

Wang, Y., Wang, Y., Wan, X., Huang, C., Wang, R., Liu, X., Yi, J., and Zhang, Y.: Influence of the Hanjiang River's Inlet Sediment Decrease on Modern Sedimentation in the Underwater Delta, Applied Sciences, 13, 8039, 10.3390/app13148039, 2023.

Warner, J. C., Sherwood, C. R., Arango, H. G., and Signell, R. P.: Performance of four turbulence closure models implemented using a generic length scale method, Ocean Modelling, 8, 81-113, 10.1016/j.ocemod.2003.12.003, 2005.

Warner, J. C., Sherwood, C. R., Signell, R. P., Harris, C. K., and Arango, H. G.: Development of a three-dimensional, regional, coupled wave, current, and sediment-transport model, Computers & Geosciences, 34, 1284-1306, 10.1016/j.cageo.2008.02.012, 2008.

Warner, J. C., Armstrong, B., He, R., and Zambon, J. B.: Development of a Coupled Ocean–Atmosphere–Wave–Sediment Transport (COAWST) Modeling System, Ocean Modelling, 35, 230-244, 10.1016/j.ocemod.2010.07.010, 2010.

Warner, J. C., Schwab, W. C., List, J. H., Safak, I., Liste, M., and Baldwin, W.: Inner-shelf ocean dynamics and seafloor morphologic changes during Hurricane Sandy, Continental Shelf Research, 138, 1-18, 10.1016/j.csr.2017.02.003, 2017.

Weatherall, P., Marks, K. M., Jakobsson, M., Schmitt, T., Tani, S., Arndt, J. E., Rovere, M., Chayes, D., Ferrini, V., and Wigley, R.: A new digital bathymetric model of the world's oceans, Earth and Space Science, 2, 331-345, https://doi.org/10.1002/2015EA000107, 2015.

Wright, L. D., and Coleman, J. M.: Variations in Morphology of Major River Deltas as Functions of Ocean Wave and River Discharge Regimes, AAPG Bulletin, 57, 370-398, 1973.

Wright, L. D., and Nittrouer, C. A.: Dispersal of river sediments in coastal seas: Six contrasting cases, Estuaries, 18, 494-508, 10.2307/1352367, 1995.

Wu, C., Xing, W., Jie, R., Yun, B., Zhigang, H., Yiaping, L., Heyin, S., and Wenyan, Z.: Morphodynamics of the rock-bound outlets of the Pearl River estuary, South China — A preliminary study, Journal of Marine Systems, 82, S17-S27, 10.1016/j.jmarsys.2010.02.002, 2010.

Wu, Z., Milliman, J. D., Zhao, D., Zhou, J., and Yao, C.: Recent geomorphic change in LingDing Bay,

China, in response to economic and urban growth on the Pearl River Delta, Southern China, Global and Planetary Change, 123, 1-12, 10.1016/j.gloplacha.2014.10.009, 2014.

Wu, Z., Milliman, J. D., Zhao, D., Cao, Z., Zhou, J., and Zhou, C.: Geomorphologic changes in the lower Pearl River Delta, 1850–2015, largely due to human activity, Geomorphology, 314, 42-54, 10.1016/j.geomorph.2018.05.001, 2018.

Wu, Z. Y., Saito, Y., Zhao, D. N., Zhou, J. Q., Cao, Z. Y., Li, S. J., Shang, J. H., and Liang, Y. Y.: Impact of human activities on subaqueous topographic change in Lingding Bay of the Pearl River estuary, China, during 1955-2013, Scientific Reports, 6, 37742, 10.1038/srep37742, 2016.

Xia, X. M., Li, Y., Yang, H., Wu, C. Y., Sing, T. H., and Pong, H. K.: Observations on the size and settling velocity distributions of suspended sediment in the Pearl River Estuary, China, Continental Shelf Research, 24, 1809-1826, 10.1016/j.csr.2004.06.009, 2004.

Xu, K., Corbett, D. R., Walsh, J. P., Young, D., Briggs, K. B., Cartwright, G. M., Friedrichs, C. T., Harris, C. K., Mickey, R. C., and Mitra, S.: Seabed erodibility variations on the Louisiana continental shelf before and after the 2011 Mississippi River flood, Estuarine, Coastal and Shelf Science, 149, 283-293, https://doi.org/10.1016/j.ecss.2014.09.002, 2014.

Xu, K., Mickey, R. C., Chen, Q., Harris, C. K., Hetland, R. D., Hu, K., and Wang, J.: Shelf sediment transport during hurricanes Katrina and Rita, Computers & Geosciences, 90, 24-39, https://doi.org/10.1016/j.cageo.2015.10.009, 2016.

Xue, Z., He, R., Liu, J. P., and Warner, J. C.: Modeling transport and deposition of the Mekong River sediment, Continental Shelf Research, 37, 66-78, 10.1016/j.csr.2012.02.010, 2012.

Yang, B., Liu, S.-M., and Zhang, G.-L.: Geochemical characteristics of phosphorus in surface sediments from the continental shelf region of the northern South China Sea, Marine Chemistry, 198, 44-55, 10.1016/j.marchem.2017.11.001, 2018.

Yang, J., Wu, D., and Lin, X.: On the dynamics of the South China Sea Warm Current, Journal of Geophysical Research: Oceans, 113, https://doi.org/10.1029/2007JC004427, 2008.

Young, I. R., Zieger, S., and Babanin, A. V.: Global trends in wind speed and wave height, Science, 332, 451-455, 10.1126/science.1197219, 2011.

Zang, Z., Xue, Z. G., Xu, K., Bentley, S. J., Chen, Q., D'Sa, E. J., and Ge, Q.: A Two Decadal (1993–2012) Numerical Assessment of Sediment Dynamics in the Northern Gulf of Mexico,

1670   Water, 11, 938, 2019.

1671   Zeng, X., He, R., Xue, Z., Wang, H., Wang, Y., Yao, Z., Guan, W., and Warrillow, J.: River-derived

1672   sediment suspension and transport in the Bohai, Yellow, and East China Seas: A preliminary

1673   modeling study, Continental Shelf Research, 111, 112-125,

1674   https://doi.org/10.1016/j.csr.2015.08.015, 2015.

1675   Zhan, W., Wu, J., Wei, X., Tang, S., and Zhan, H.: Spatio-temporal variation of the suspended sediment

1676   concentration in the Pearl River Estuary observed by MODIS during 2003–2015, Continental

1677   Shelf Research, 172, 22-32, 10.1016/j.csr.2018.11.007, 2019.

1678   Zhang, G., Cheng, W., Chen, L., Zhang, H., and Gong, W.: Transport of riverine sediment from

1679   different outlets in the Pearl River Estuary during the wet season, Marine Geology, 415, 105957,

1680   10.1016/j.margeo.2019.06.002, 2019.

1681   Zhang, G., Chen, Y., Cheng, W., Zhang, H., and Gong, W.: Wave Effects on Sediment Transport and

1682   Entrapment in a Channel-Shoal Estuary: The Pearl River Estuary in the Dry Winter Season,

1683   Journal of Geophysical Research: Oceans, 126, 10.1029/2020jc016905, 2021.

1684   Zhang, G., Hu, P., Hu, S., Zhang, H., and Gong, W.: Tidal effects on the dispersal and water age of the

1685   plumes from eight outlets of the Pearl river during the wet summer, Ocean & Coastal Management,

1686   266, 107704, https://doi.org/10.1016/j.ocecoaman.2025.107704, 2025.

1687   Zhang, J., Jiang, Q., Jeng, D., Zhang, C., Chen, X., and Wang, L.: Experimental Study on Mechanism

1688   of Wave-Induced Liquefaction of Sand-Clay Seabed, Journal of Marine Science and Engineering,

1689   8, 66, 10.3390/jmse8020066, 2020.

1690   Zhang, W., Wei, X., Zheng, J., Zhu, Y., and Zhang, Y.: Estimating suspended sediment loads in the

1691   Pearl River Delta region using sediment rating curves, Continental Shelf Research, 38, 35-46,

1692   10.1016/j.csr.2012.02.017, 2012.

1693   Zhang, W., Zheng, J., Ji, X., Hoitink, A. J. F., van der Vegt, M., and Zhu, Y.: Surficial sediment

1694   distribution and the associated net sediment transport pattern retain-->in the Pearl River Estuary,

1695   South China, Continental Shelf Research, 61-62, 41-51, 10.1016/j.csr.2013.04.011, 2013.

1696   Zhang, Y. J., Ye, F., Stanev, E. V., and Grashorn, S.: Seamless cross-scale modeling with SCHISM,

1697   Ocean Modelling, 102, 64-81, https://doi.org/10.1016/j.ocemod.2016.05.002, 2016.

1698   Zhong, Y., Chen, Z., Li, L., Liu, J., Li, G., Zheng, X., Wang, S., and Mo, A.: Bottom water

1699   hydrodynamic provinces and transport patterns of the northern South China Sea: Evidence from

1700   grain size of the terrigenous sediments, Continental Shelf Research, 140, 11-26,

1701   10.1016/j.csr.2017.01.023, 2017.

1702 Zong, X., Cheng, X., Zhang, S., Lian, Q., Deng, F., and Chen, Z.: Tidal effects on dynamics and

1703   freshwater transport of a medium-scale river plume with multiple outlets, Ocean Modelling, 188,

1704   102338, https://doi.org/10.1016/j.ocemod.2024.102338, 2024.

1705 Zong, Y., Huang, K., Switzer, A., yu, F., and Yim, W.: An evolutionary model for the Holocene

1706   formation of the Pearl River delta, China, The Holocene, 19, 129-142,

1707   10.1177/0959683608098957, 2009.

1708